Birth of a large volcanic edifice offshore Mayotte via lithosphere-scale dyke intrusion

Nathalie Feuillet [1✉], Stephan Jorry[2], Wayne C. Crawford[1], Christine Deplus [1], Isabelle Thinon [3], Eric Jacques[1], Jean Marie Saurel[1], Anne Lemoine[3], Fabien Paquet [3], Claudio Satriano [1], Chastity Aiken[2], Océane Foix[1,8], Philippe Kowalski[1], Angèle Laurent [1], Emmanuel Rinnert[2], Cécile Cathalot [2], Jean-Pierre Donval[2], Vivien Guyader [2], Arnaud Gaillot[2], Carla Scalabrin [2], Manuel Moreira[1,9], Aline Peltier [1], François Beauducel[1,4], Raphaël Grandin [1], Valérie Ballu [5], Romuald Daniel[1], Pascal Pelleau[2], Jérémy Gomez[1], Simon Besançon[1], Louis Geli [2], Pascal Bernard[1], Patrick Bachelery[6], Yves Fouquet [2], Didier Bertil[3], Arnaud Lemarchand [1] and Jérome Van der Woerd[7]

Volcanic eruptions shape Earth's surface and provide a window into deep Earth processes. How the primary asthenospheric melts form, pond and ascend through the lithosphere is, however, still poorly understood. Since 10 May 2018, magmatic activity has occurred offshore eastern Mayotte (North Mozambique channel), associated with large surface displacements, very-low-frequency earthquakes and exceptionally deep earthquake swarms. Here we present geophysical and marine data from the MAYOBS1 cruise, which reveal that by May 2019, this activity formed an 820-m-tall, ~5 km³ volcanic edifice on the sea-floor. This is the largest active submarine eruption ever documented. Seismic and deformation data indicate that deep (>55 km depth) magma reservoirs were rapidly drained through dykes that intruded the entire lithosphere and that pre-existing subvertical faults in the mantle were reactivated beneath an ancient caldera structure. We locate the new volcanic edifice at the tip of a 50-km-long ridge composed of many other recent edifices and lava flows. This volcanic ridge is an extensional feature inside a wide transtensional boundary that transfers strain between the East African and Madagascar rifts. We propose that the massive eruption originated from hot asthenosphere at the base of a thick, old, damaged lithosphere.

Since 10 May 2018, Mayotte Island (Comoros archipelago, Indian Ocean, Fig. 1a) has experienced a major magmatic event off its eastern coast. This event generated more than 11,000 detectable earthquakes (up to moment magnitude (M_w) 5.9), surface deformation rates of up to 200 mm yr^{-1} and unusual very-low-frequency (VLF) earthquakes[1–3]. As of May 2021 (the time of writing), Mayotte is still deforming, and both VLF events and earthquakes up to M_w 4 are still being recorded.

Before this event, no recent eruption or notable seismic activity was reported around Mayotte[2]. Only two earthquakes were detected within 100 km of the island since 1972[4], and the most recent volcanic exposure is a pumice layer from 4–6 thousand years ago (ka) sampled in the lagoon surrounding the island[5].

Recent geodynamic reconstructions suggest that the Comoros archipelago was built on ~150 Ma oceanic lithosphere accreted to accommodate the opening of the Western Somali Basin[6]. The Comorian volcanism may result from partial melting of the base of this old lithosphere in interaction with plume material[7–9], possibly super plumes originating from Africa[10–12], and may have been controlled by lithospheric deformation[13,14]. Subaerial volcanic activity on Mayotte Island began 11 Ma[13]. Well-preserved cones, tuff

rings and maar craters in the northeastern part of the island (on Petite-Terre and in and around Mamoudzou[7,15] and further offshore[16] (Fig. 1b)) testify to relatively recent (probably Holocene[7]) subaerial explosive volcanic activity. Gas emissions on Petite-Terre indicate magma degassing[17].

The discovery of the eruption and the new volcanic edifice
To determine the origin of the seismicity and deformation and to search for any seafloor volcanic activity, we deployed ocean-bottom seismometers (OBSs) with attached absolute pressure gauges (APGs) and acquired high-resolution marine data (bathymetry, seafloor and water-column backscatter), rock dredges and conductivity–temperature–depth (CTD) rosette during the MAYOBS1 (2–19 May 2019) cruise aboard the RV *Marion Dufresne*[18].

A systematic 12 kHz multibeam echosounder survey revealed a 820-m-tall new volcanic edifice (NVE) 50 km east of Mayotte (Fig. 1). The NVE was detected by comparing our data to those acquired during a 2014 survey by the French Naval Hydrographic and Oceanographic Service (SHOM)[19] (Fig. 2a). The edifice sits on an area that, in the 2014 seafloor topography, was locally almost flat at around 3,300 m below sea level.

[1]Université de Paris, Institut de physique du globe de Paris, CNRS, Paris, France. [2]IFREMER, Unité Géosciences Marines, Technopole La Pointe du Diable, Plouzané, France. [3]Bureau de Recherches Géologiques et Minières—BRGM, DGR/GBS, Orléans, France. [4]Université Grenoble Alpes, IRD, ISterre, Grenoble, France. [5]LIttoral ENvironnement et Sociétés (LIENSs) UMR7266, Université de La Rochelle—CNRS, La Rochelle, France. [6]Université Clermont Auvergne, CNRS, IRD, OPGC, Laboratoire Magmas et Volcans, Clermont-Ferrand, France. [7]Institut de Physique du Globe de Strasbourg UMR7516 CNRS Université de Strasbourg, Strasbourg, France. [8]Present address: Montpellier 2 University, Montpellier, France. [9]Present address: Orleans University, Orleans, France. ✉e-mail: feuillet@ipgp.fr
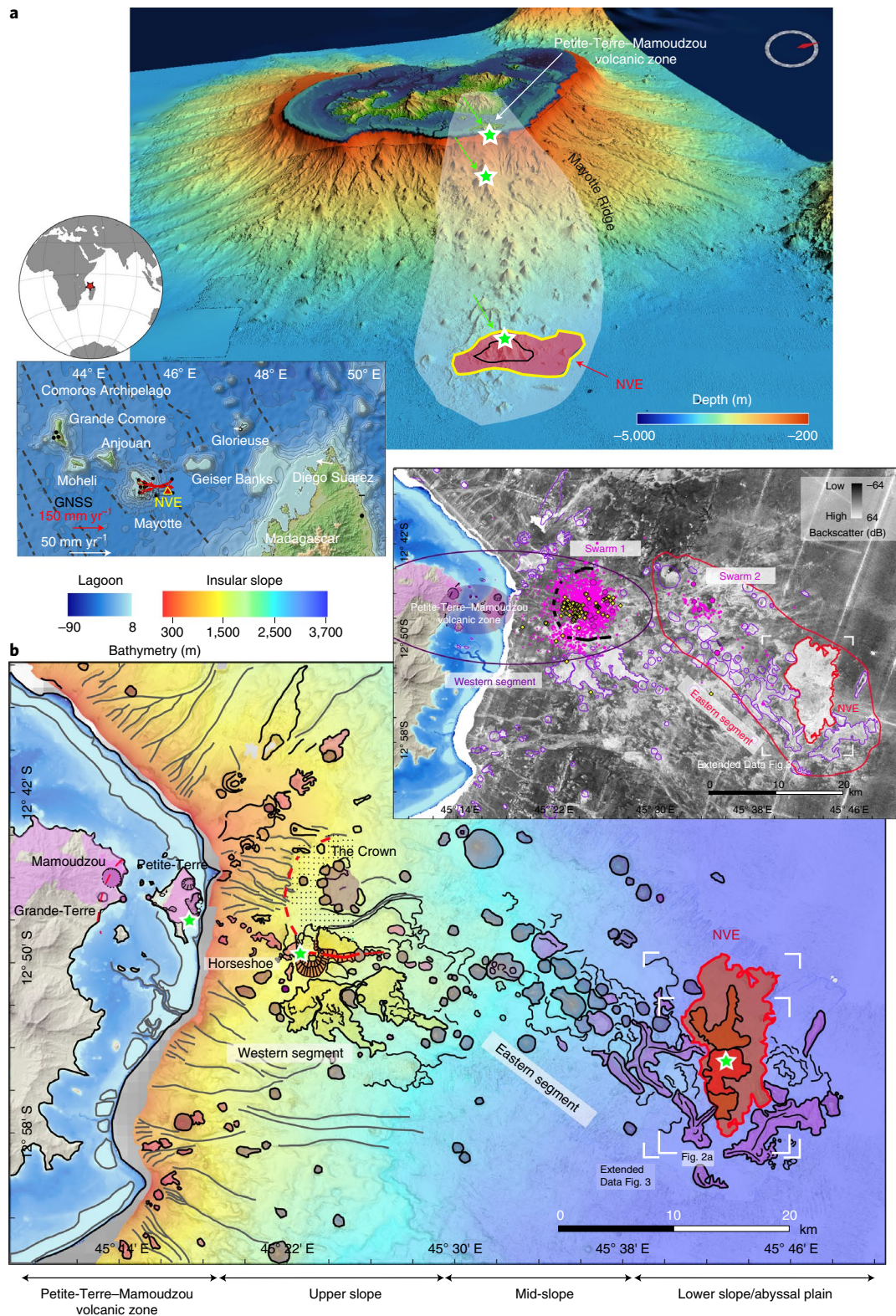
Fig. 1 | The volcanic ridge offshore Mayotte. a, Three-dimensional (3D) Westward view of Mayotte Island and insular slope (threefold vertical exaggeration for the topography and bathymetry). Green stars represent acoustically detected plumes above the Horseshoe, the NVE and the degassing area on Petite-Terre Island. Left inset: geographic setting and GNSS surface horizontal displacements stations. Black points represent seismic stations. Dashed grey lines represent Mesozoic fracture zones[6]. **b**, Geological interpretations of MAYOBS1 data. Purple patches represent volcanic structures (mainly cones). Pink patches represent lava flows and elongated features. Yellow patches represent the upper slope's high reflective lava flows. NVE is in red (central part) and orange (radial ridges and flat flows). Green stars are as in **a**. Red lines represent fissures and faults; dashed lines are inferred faults; black dots mark a bathymetric depression; white boxes show locations of Fig. 2a and Extended Data Fig. 3. Right Inset: as in **b** with MAYOBS backscatter data. Pink dots represent OBS seismicity; yellow diamonds mark locations of the VLF earthquakes; the white box shows location of Extended Data Fig. 3.
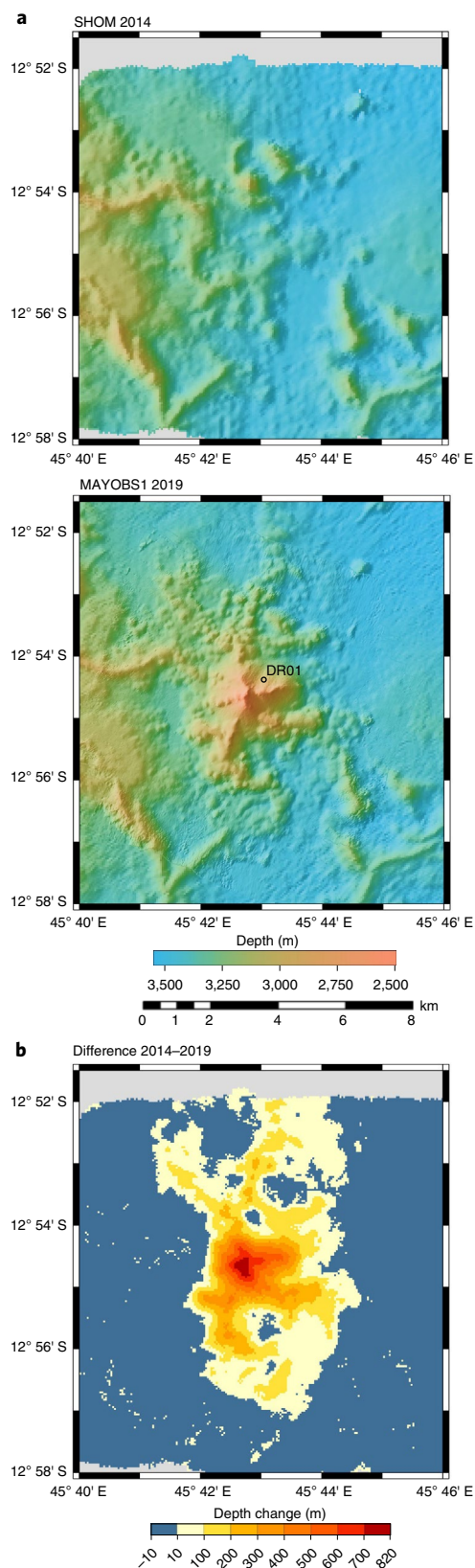
Fig. 2 | The NVE offshore Mayotte. a, Thirty-metre-resolution bathymetric maps from shipboard EM122 multibeam, illuminated from N 290° E. Upper panel: SHOM bathymetry collected in 2014[19]; lower panel: MAYOBS1 bathymetry collected in May 2019[18]. The black circle is the position of dredge DR01. **b**, Depth changes between 2014 and 2019. The change in topography is estimated to be significant when larger than 10 m.

The NVE has grown on the lower insular slope of Mayotte, at the eastern tip of a west-northwest–east-southeast-trending volcanic ridge (Mayotte ridge) on the submarine flank of Mayotte (Fig. 1). The NVE and many other volcanic features along the ridge have high acoustic reflectivity compared with the surrounding sediments, indicating recent volcanic activity all along the ridge (right inset of Fig. 1b and Extended Data Figs. 1, 2, and 3). The ridge is 50 km long, extending from the most recent subaerial cones and maar craters on Grande-Terre and Petite-Terre Islands (MPT volcanic zone) to the NVE (Fig. 1b). It is divided into two main segments, one on the upper slope (western) and one on the mid- to lower slope (eastern). The eastern segment trends N 130° E and is made of many constructional features similar to mafic submarine eruption features observed elsewhere:[20–22] cones up to 2 km wide and 500 m high, probably monogenetic, and lava flows with smooth bathymetry, elongated ridges with steep slopes and varying orientations, which could result from dykes in more sedimented areas (Fig. 1 and Extended Data Fig. 2d,e).

The western segment is made of volcanic features having more-complex morphologies and emplaced along different directions (Fig. 1b and Extended Data Fig. 2b,c). The main features are (1) two N 40° E- and N 120° E-trending sets of high-backscatter cones and lava flows, northeast and southeast of Petite-Terre, respectively. These sets converge towards the onshore maar craters of Petite-Terre and may have been emplaced along pre-existing fractures or faults; (2) a horseshoe-shaped edifice (the Horseshoe) with a 3.5-km-wide cone, steep slopes and a large collapse-induced scar (east of the Horseshoe, several smaller cones and volcanic features are aligned east–west, suggesting eruptive fissures; large lava flows originate from this fissure system); (3) a 4-km-wide circular structure (the Crown), whose rim is crowned by seven 1-km-wide, 100- to 150-m-high volcanic cones. Their arrangement suggests typical post-caldera domes[23]. West of the Crown, submarine canyons and slope failure scars terminate at a north–south-trending slope break that may be controlled by faulting. The Crown appears to sit inside a larger 10-km-wide flat depression, bounded by faults and fissures, which could be the remnant of an ancient caldera collapse.

The NVE is located at the eastern tip of the eastern segment of the Mayotte ridge (Fig. 1b). In May 2019, its summit rose to 2,580 m below sea level. Its central peak resembles a pyramid with steep and smooth slopes (Fig. 2a and Extended Data Fig. 3). Radial ridges, up to 300 m thick and extending up to 5 km from the central pyramid, display hummocky morphology similar to that observed along mid-ocean volcanic ridges[24] and active seamounts[22] and probably correspond to coalesced pillow-lava mounds[21]. Beyond and between the hummocky ridges, flat areas up to 100 m thick, with high backscatter, could indicate channelized lava flows or sheet flows emplaced at high effusion rates[25]. We calculate the volume of material corresponding to the 2014–2019 seafloor depth difference to be at least $5.0 \pm 0.3\,km^3$ (Fig. 2b). Popping fragments of very fresh basanitic pillow lavas (SiO_2, 47 wt%; $Na_2O + K_2O$, 7.1 wt%; MgO, 5.7 wt%[26]) were dredged on the northeastern flank of the NVE, near its summit (see Fig. 2a for sample location and Supplementary Section 1). The lavas, similar to other basanites sampled in northern Mayotte[7], are aphyric with rare microphenocrysts of olivine (Fo70) and Ti-magnetite.

An ~1,900-m-high vertical acoustic plume, rising through the water column from the NVE summit to ~800 m below the sea surface, was imaged several times during the cruise using the ship-borne multibeam echosounder (Fig. 3 and Supplementary Movie 1). A vertical CTD rosette cast to 3,137 m depth above the northern flank of the NVE, 1,000 m offset from the summit, showed strong geochemical signatures. Elevated concentrations of volatiles ($H_2 = 550\,nM$, $CH_4 = 831\,nM$, $CO_2 = 34\,\mu M$), high turbidity and high total alkalinity values were associated with temperature and pH anomalies (respectively, 0.2 °C and 1 pH unit[27]; Extended Data Fig. 4). Such chemical
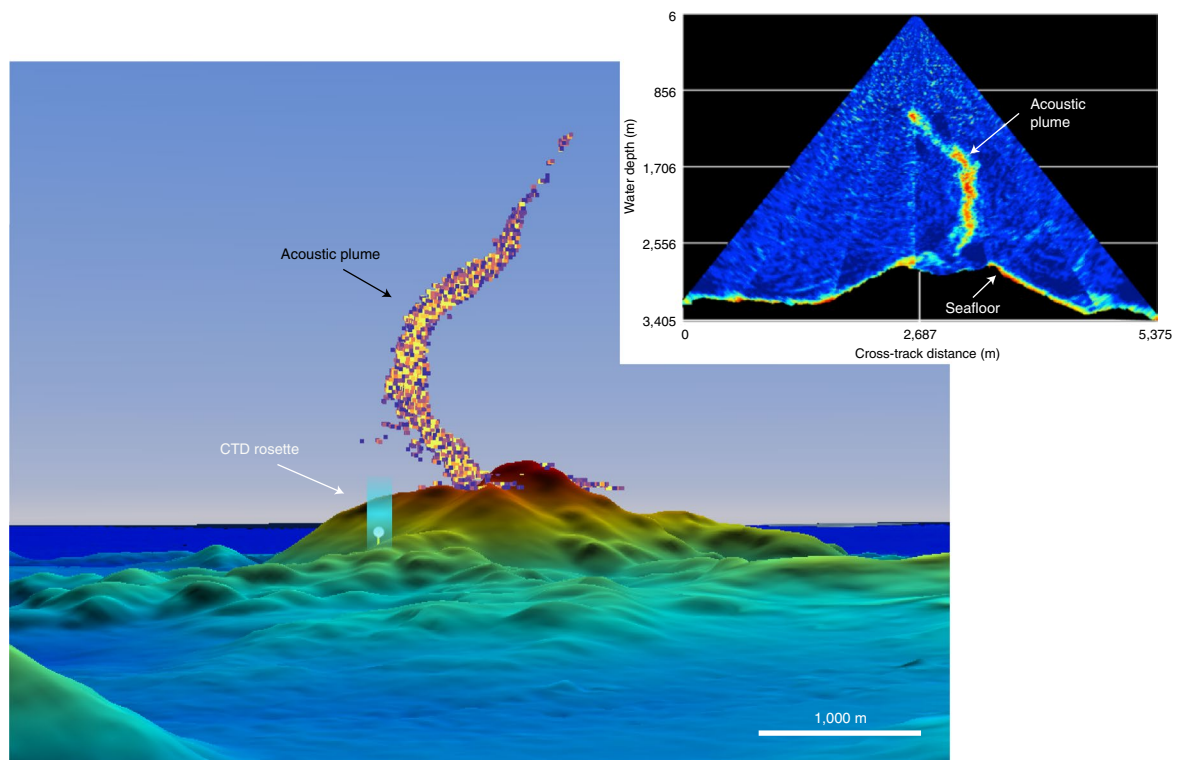
Fig. 3 | The NVE and the acoustic plume. a, Southward 3D view of the NVE and the water-column acoustic plume observed one hour before the CTD rosette on 16 May 2019. The white dot and blue patch indicate the position of the CTD rosette deployment, 1 km from the summit of the volcano. Right inset: processed polar echogram from one EM122 multibeam ping on 16 May 2019 (13:33 UT).

anomalies are characteristic of submarine eruptions and may reflect magma degassing[28], molten lava interaction with seawater[29] or fluid/water discharge from subsurface storage zones in the crust or sedimentary cover[30]. The height and the strong backscatter signature of the acoustic plume suggest that a mixture of solid particles (pyroclastic/hyaloclastic jet[28]) and/or differentiated fluid phases (droplets, hydrate-coated bubbles or free gas[31]) are driven upwards through the water column from the NVE summit[32]. High turbidity measured at water depths below 2,500 m, on the northern flank of the NVE, probably indicates the presence of these particles[33]. Both the multiple observations of the vertical acoustic plume at the summit of the NVE and the high H_2 concentration 1 km away indicate that the eruption was probably ongoing in May 2019[29].

In the upper-slope zone, 30 km from the volcano, two ~1,000-m-high acoustic plumes were detected above the Horseshoe edifice (Fig. 1, Extended Data Fig. 5 and Supplementary Movie 2), but no significant changes in seafloor morphology or reflectivity were detected.

The seismicity and VLF events relocated by OBS data

The combined land–OBS network of seismic stations (Supplementary Fig. 2.1) detected 17,000 events between 25 February and 6 May 2019. We manually relocated about 800 of the largest earthquakes on board (Methods and Supplementary Section 2). Ninety-four percent of the earthquakes cluster beneath the western segment of the Mayotte ridge, 40 km west of the NVE and 5–15 km east of Petite-Terre (right inset of Fig. 1b, swarm 1). Almost all of the remaining events form a secondary swarm beneath the northwestern tip of the eastern segment, 30 km from Petite-Terre and 20 km from the NVE (right inset of Fig. 1b, swarm 2). A few events are also scattered along the eastern segment. We searched the full OBS–land catalogue for events beneath the NVE but found none. The located earthquakes are all

very deep, ranging from 25 ± 5 to 50 ± 5 km. In addition, all P–S arrival delays recorded by an OBS deployed for 48 h above the main swarm were greater than 3 s, indicating no events less than 20 km depth (Fig. 4, Extended Data Fig. 6b, Methods and Supplementary Section 2.2). The land–OBS catalogue does not show any evidence for seismicity migration, but it represents only a two-month 'snapshot' of the activity. To extend the observational time window, we relocated 139 earthquakes recorded by the land stations between May 2018 and the first OBS deployment. All the events were beneath the volcanic ridge (Extended Data Fig. 6a). During the first weeks of the crisis, they were located mainly beneath the northwestern tip of the eastern segment, between 30 and 50 km depth, whereas in the last two weeks of June, a few events occurred closer to the NVE and between 30 km depth and the surface.

In addition to the high-frequency seismicity, VLF events were recorded by the OBSs wideband hydrophones. Their waveforms are similar to those of the globally detected 11 November 2018 event (exponentially decaying monochromatic signals of approximately 2,000 s duration, with dominant period of ~15 s and polarized Rayleigh waves), suggesting repeated excitation of the same radiating source. We located 84 VLF events using waveform cross-correlation (Methods and Supplementary Section 2.3); all of them are probably above seismic swarm 1 (Fig. 4 and Extended Data Fig. 6b), at a mean depth of 22 ± 15 km.

GNSS data and APG modelling

The Global Navigation Satellite System (GNSS) network includes nine stations on Mayotte Island and two far field stations at Diego Suarez and Grande Glorieuse Islands. The geometry is not optimal, preventing geodetic inversions for complicated structures or media. We performed Bayesian inversions[34] of the data using a point source in an elastic half space with two distinct analytical formalisms: an
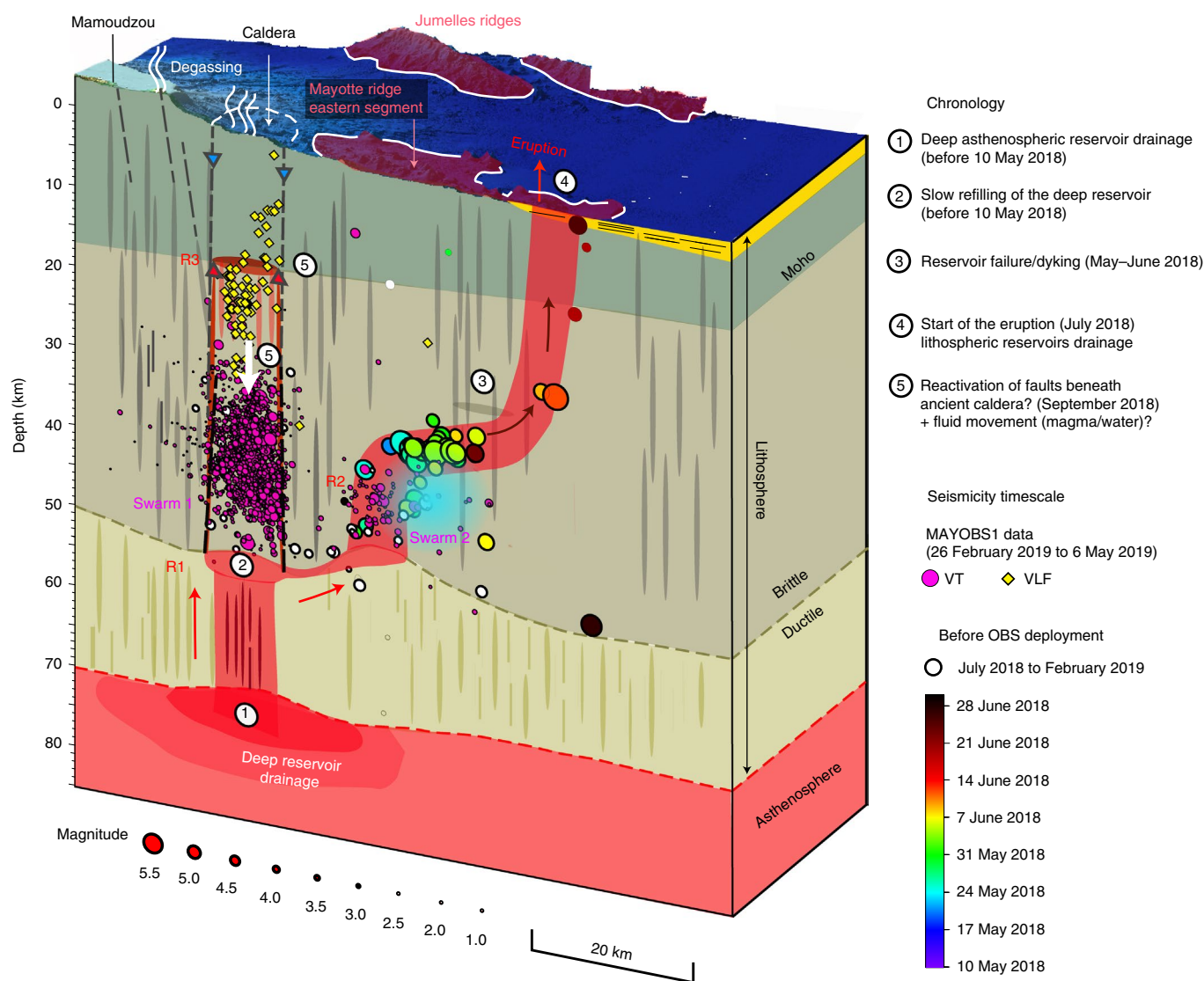
Fig. 4 | Conceptual model of the submarine eruption offshore Mayotte. Bathymetry as in Fig. 1b, no vertical exaggeration. Purple zones represent N130° E volcano–tectonic ridges and segments. Dashed white lines are the inferred ancient caldera with degassing zones above. Cross-section: red and reddish zones represent magma storage zones (mush or magma chambers) and magma pathways involved in the 2018–2020 Mayotte volcanic crisis and seafloor eruption; yellow layer represents sediments; dashed lines are subvertical faults beneath inferred caldera possibly reactivated by the deflation of a deep reservoir; white arrow is a possible downsag at an initial stage of caldera collapse; pink dots represent 800 volcano-tectonic (VT) earthquakes located using OBSs and land stations. The other dots are 139 earthquakes from before the OBS deployment: coloured dots are from the first six weeks of the crisis and white dots are from the remaining eight months before the OBS deployment. Yellow diamonds are VLF earthquakes. Blue and red triangles represent water and magma movements, respectively. The blue patch is the location, with 3σ uncertainties, of the most robust isotropic source deformation model. Moho depth is from ref. [37]. Lithosphere/asthenosphere boundary depth is from refs. [60,61].

isotropic point source[35] and a point compound dislocation model (pCDM[36]; Methods, Supplementary Section 3 and Extended Data Fig. 7). In both cases, the results indicate ~5-km³-deflation of a deep reservoir (>30 km). The simplest and most robust model is the deflation of an ~40-km-deep isotropic source below the eastern segment of the Mayotte ridge. An increase in absolute seafloor pressure measured by all APGs on the OBS frames, interpreted as seafloor subsidence, is compatible with these models (Methods, Supplementary Section 3.2 and Extended Data Fig. 7d).

Magma reservoirs and chronology of the eruption

Most of our located seismicity and modelled GNSS sources lie in the lithospheric mantle, beneath the ~17-km-deep Moho[37]. Volcanic

seismicity this deep is rarely documented[38,39], especially in dense swarms during eruptions.

The distribution of the seismicity in the first weeks of the crisis suggests a dyke migration from the mid-slope zone to the NVE, along the eastern segment of the Mayotte ridge. This is also supported by the migration of the largest earthquakes' centroid-moment-tensor depths[40] towards the surface (Extended Data Figs. 6c and 8) and agrees well with refs. [1,2]. The earthquakes show strike-slip focal mechanisms compatible with a least compressive principal stress orthogonal to the eastern segment of the ridge. Similar stress trends have been observed during dyking events beneath the Izu Peninsula in Japan[41] and in Iceland[42] but at much shallower depths, where they were interpreted as seismic shear faulting caused by stress trans-
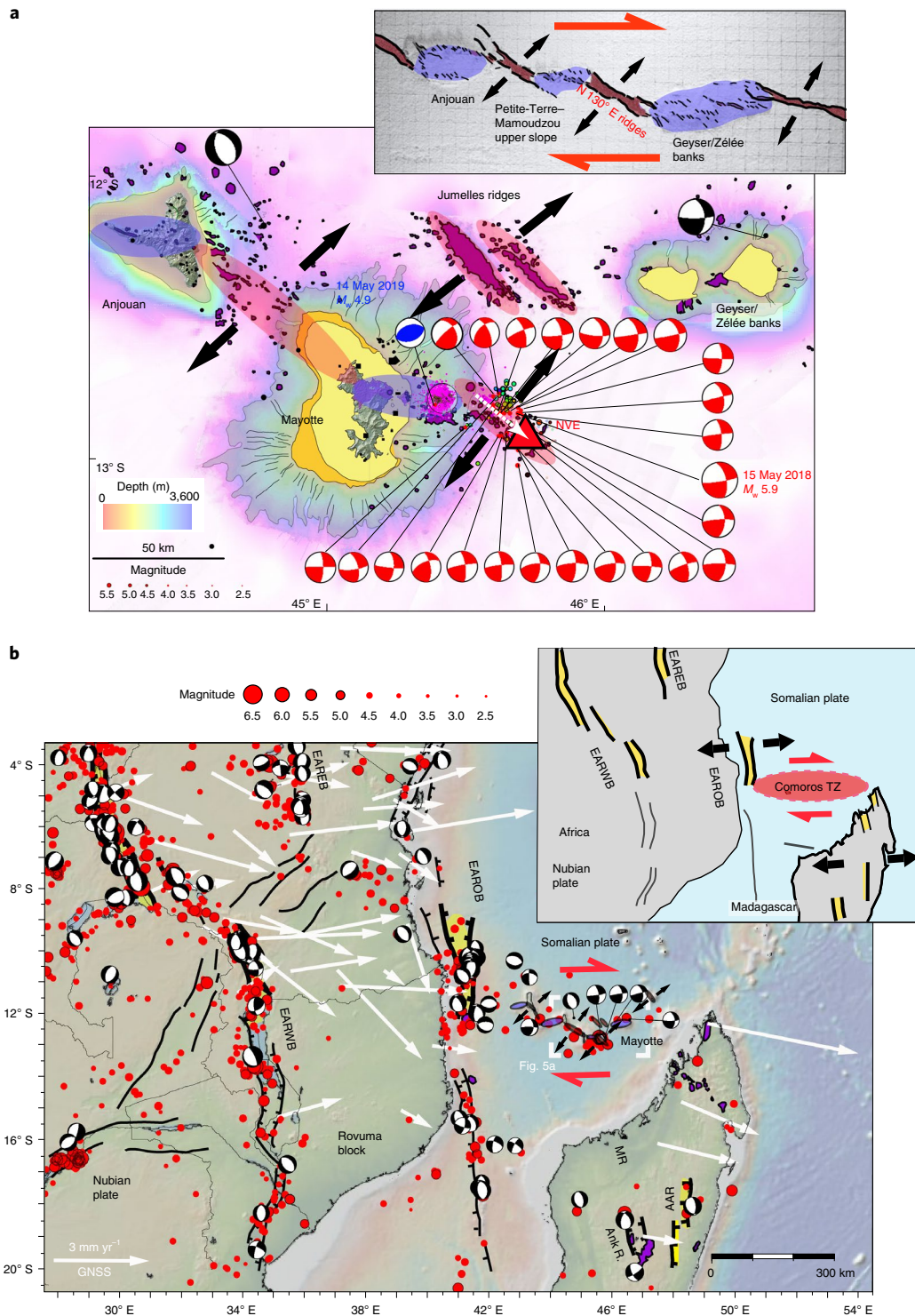
Fig. 5 | Regional volcano–tectonic setting of the submarine eruption offshore Mayotte. a, Volcano–tectonic setting of the NVE. Volcanic cones and ridges (purple) from this study and refs. [13,16,51,71]. Dots and diamonds are earthquakes as in Fig. 4 and Extended Data Figs. 6 and 8. Focal mechanisms are for $M > 5$ earthquakes[40]. Dotted white arrow is dyking intrusion along eastern segment of the Mayotte volcanic ridge; red ellipse is inferred main volcano–tectonic ridges; purple ellipses represent highly damaged zones between the en echelon ridges; thick black arrows show local extension direction. Inset: sandbox model adapted from ref. [58] illustrating the possible arrangement of the main volcano–tectonic structures in Comoros. **b**, Geodynamic setting of the East African rift systems. Main tectonic structures and extensional zones in Africa (EAREB, EARWB and EAROB represent the East African Rift East, West and Offshore branches, respectively) and Madagascar (Ank. R, AAR and MR represent the Ankarata, Alaotra –Ankay and Mahajanga rifts) are from this study and refs. [56,57,72–74]. Purple patches represent Quaternary volcanism in Madagascar[57]; red dots are $M > 2.5$ earthquakes[4] with focal mechanisms from ref. [40] for the $M > 5$ earthquakes; arrows show GNSS horizontal motions[72]; small purple ellipses in the Comoros are as in **a** with double dark red arrows representing the volcanic ridge east of Mayotte and extension direction. Inset: simplified tectonic map of the East African rift system: yellow highlights represent the most active rifts and graben; the red ellipse is the transfer zone (TZ) of the Comoros with direction of lateral motion.

fer to the surrounding vertical faults in response to dyke opening and propagation.

During the first six weeks of the crisis, the magma migrated 20 km laterally along the eastern segment of the Mayotte ridge, then upward (Fig. 4 and Extended Data Fig. 8). The building of the NVE may have begun in July 2018 once the dyke reached close to the surface[1,2], allowing for high magma flow rates and rapid ensuing growth. On the basis of this assumption, we estimate a minimum mean lava flow rate of ~180 m^3 s^{-1} between the start of the eruption on the seafloor and our survey (~11 months). The local stress probably decreased considerably once the magma path to the NVE was opened, as is observed during many eruptions involving dyke propagation[43], which would explain why no earthquakes were detected beneath the NVE during the OBS deployment.

After the dyke reached the near surface, seismicity resumed beneath the mid- and upper-slope volcanic zones (Fig. 4 and Extended Data Figs. 6a,b and 8), and its pattern appears to be constant since September 2018[2]. This stationary seismicity could be caused by stress perturbation along pre-existing structures and/or fluid (gas, magma or water) motions. The swarm 1 earthquakes cluster beneath the ancient caldera structure inferred from our high-resolution bathymetry (right inset of Fig. 1b and Extended Data Figs. 6b and 8). This seismicity could indicate activation of pre-existing subvertical faults[44] above a deep (>55 km) depleting reservoir (R1, Fig. 4), as has been observed during caldera collapse events:[45] if so, these faults would be much deeper than documented elsewhere. Analogue models for collapse of a caldera with a high roof aspect ratio (thickness/width >> 1) indicate reverse fault motions during an initial downsag stage[46], in agreement with the focal mechanism of the 14 May 2019 M_w 4.9 swarm 1 region earthquake[1] (Fig. 4 and Extended Data Fig. 8).

The VLF events located above swarm 1 may be generated by the resonance of a fluid-filled (magma, gas or hydrothermal) shallower cavity or a fluid-filled crack, probably at the base of the crust. The characteristic frequency and duration of these events are very different from VLF events typically observed in volcanic zones, for example[47]. Simple up-scaling of fluid resonance models[48,49] implies a shallower reservoir size of several kilometres (R3, Fig. 4). The excitation mechanism could be rapid slip and related strain on faults close to the reservoir or episodic collapse of a piston at the base of this shallow reservoir[47]. The acoustic plumes emanating from the overlying Horseshoe edifice may result from actively degassing this shallower reservoir.

Both the distribution of seismicity over time and the surface deformation models suggest the drainage of an exceptionally deep reservoir by a dyke that propagated from the base of the brittle lithosphere to the eastern portion of the Mayotte ridge, possibly intersecting another vertical storage zone below seismic swarm 2 (R2, Fig. 4 and Extended Data Fig. 8) before reaching the surface. Within the uncertainties, the GNSS isotropic model may reflect the drainage of reservoir R2 in the brittle lithosphere. The deeper reservoir (R1) may have slowly recharged from the asthenosphere before reaching tensile failure in May 2018[50].

Magma roots and paths
The eastern segment of the Mayotte ridge, along which the dyke propagated, has the same orientation as many other volcanic features over a range of scales (Quaternary dykes, volcanic vent alignments, ridges and volcanic rift zones) in the northeastern part of Mayotte Island[15] and in and around the other Comoros Islands[13,51] (Fig. 5a and Extended Data Fig. 9). The left-lateral en echelon arrangement of these features resembles that of extensional tectonic structures in a context of oblique extension (in segmented and diffuse strike-slip fault systems[52] or highly oblique rifting (for example, refs. [53–55]). We infer that the Mayotte ridge results from the interplay between volcanism and tectonics. The location and orientation of the volcanic features may be in part controlled by the pre-existing Mesozoic fracture zones[6], but they probably also emplace along new tectonic structures. These tectonic structures are extensional (fissures or step-overs) and open as a result of volcano–tectonic interactions in a wide east–west striking zone to transfer the strain between the north–south striking offshore branches of the East African rift[56] and the grabens of Madagascar (Aloatra and Ankai)[57] (Fig 5b). In this context, high strain rate[54] or highly damaged zones may develop[58] may develop (Fig. 5a inset) between the main en echelon extensional structures. Such zones may constitute high-permeability zones where large magmatic reservoirs can develop. The main Comoros volcanic islands may have grown above such zones.

Between Mayotte and Madagascar, the lithosphere–asthenosphere boundary is a sharp limit between a high-velocity 150 Ma lithosphere and a low-velocity asthenosphere, at about 70 km depth[59,60]. The low-velocity asthenosphere is interpreted as hot material spreading beneath the Mascarene basin and beyond[61]. Heating of the base of the oceanic lithosphere damaged by extensional tectonics and loaded by Mayotte Island[62] may favour the ponding of large volumes of buoyant melts. Pore-pressure increase in these zones may in turn favour failure of deep reservoirs and faults inside the brittle lithosphere.

The largest eruption ever documented in submarine domain
The NVE extruded volume (as of May 2019) is 30–1,000 times larger than that estimated for other deep-sea eruptions[21,25,63,64]. It is difficult to evaluate the dense-rock equivalent (DRE) volume[20], but taking an upper bound of 50% for the DRE factor[65], compatible with the 40% vesicularity of our rock sample[26], the DRE erupted volume could be as large as 2.5 km^3, which is larger than the 1.2–1.5 km^3 Havre silicic eruption[66], previously considered to be the largest documented submarine eruption. It would be 2.5 times larger than the Bardabunga eruption (Iceland's largest eruption of the past two centuries)[43] and only 6 times less than Iceland's 1783–1784 Laki eruption, considered to be one of the largest basaltic eruptions witnessed by humanity[67]. The volumes and flux of emitted lava during the Mayotte magmatic event are comparable to those observed during eruptions at Earth's largest hotspots (Hawaii, Iceland[43,68], and one quarter of that emplaced yearly over the entire mid-ocean-ridge system (mean estimate from spreading rates over the past 80 Myr[69]). It thus represents a considerable input in terms of CO_2 flux[70].

Future scenarios could include a new caldera collapse, submarine eruptions on the upper slope or onshore eruptions. Large lava flows and cones on the upper slope and onshore Mayotte indicate that this has occurred in the past. Since the discovery of the NVE, an observatory has been established to monitor activity in real time (REVOSIMA[3]), and return cruises continue to follow the evolution of the eruption and edifices.

Online content
Any methods, additional references, Nature Research reporting summaries, source data, extended data, supplementary information, acknowledgements, peer review information; details of author contributions and competing interests; and statements of data and code availability are available at https://doi.org/10.1038/s41561-021-00809-x.

References
1. Cesca, S. et al. Drainage of a deep magma reservoir near Mayotte inferred from seismicity and deformation. *Nat. Geosci.* **13**, 87–93 (2020).

2. Lemoine, A. et al. The 2018–2019 seismo-volcanic crisis east of Mayotte, Comoros islands: seismicity and ground deformation markers of an exceptional submarine eruption. *Geophys. J. Int.* **223**, 22–44 (2020).

3. *Bulletin de l'Activité Sismo-Volcanique à Mayotte* Report no. 2680-1205 (REVOSIMA, 2020).

4. *Search Earthquake Catalog* (USGS, 2019); https://earthquake.usgs.gov/earthquakes/search

5. Zinke, J., Reijmer, J. & Thomassin, B. Systems tracts sedimentology in the lagoon of Mayotte associated with the Holocene transgression. *Sediment. Geol.* **160**, 57–79 (2003).

6. Phethean, J. J. et al. Madagascar's escape from Africa: a high-resolution plate reconstruction for the Western Somali Basin and implications for supercontinent dispersal. *Geochem. Geophys. Geosyst.* **17**, 5036–5055 (2016).

7. Pelleter, A.-A. et al. Melilite-bearing lavas in Mayotte (France): an insight into the mantle source below the Comores. *Lithos* **208-209**, 281–297 (2014).

8. Class, C., Goldstein, S. L., Altherr, R. & Bachèlery, P. The process of plume–lithosphere interactions in the ocean basins—the case of Grande Comore. *J. Petrol.* **39**, 881–903 (1998).

9. Claude-Ivanaj, C., Bourdon, B. & Allègre, C. J. Ra–Th–Sr isotope systematics in Grande Comore Island: a case study of plume–lithosphere interaction. *Earth Planet. Sci. Lett.* **164**, 99–117 (1998).

10. Ebinger, C. J. & Sleep, N. Cenozoic magmatism throughout east Africa resulting from impact of a single plume. *Nature* **395**, 788–791 (1998).

11. Reiss, M., Long, M. & Creasy, N. Lowermost mantle anisotropy beneath Africa from differential SKS-SKKS shear-wave splitting. *J. Geophys. Res. Solid Earth* **124**, 8540–8564 (2019).

12. Class, C., Goldstein, S. L., Stute, M., Kurz, M. D. & Schlosser, P. Grand Comore Island: a well-constrained "low ³He/⁴He" mantle plume. *Earth Planet. Sci. Lett.* **233**, 391–409 (2005).

13. Nougier, J., Cantagrel, J. & Karche, J. The Comores archipelago in the western Indian Ocean: volcanology, geochronology and geodynamic setting. *J. Afr. Earth Sci.* **5**, 135–145 (1986).

14. Michon, L. in *Active Volcanoes of the Southwest Indian Ocean* (eds Bachelery, P. et al.) 233–244 (Springer, 2016).

15. Nehlig, P. et al. *Report on the French Geological Map (1/30 000)* Mayotte Sheet no. 1179 (BRGM, 2013).

16. Audru, J.-C., Guennoc, P., Thinon, I. & Abellard, O. Bathymay : la structure sous-marine de Mayotte révélée par l'imagerie multifaisceaux. *Comptes Rendus Geosci.* **338**, 1240–1249 (2006).

17. Sanjuan, B. et al. *Estimation du Potentiel Géothermique de Mayotte: Phase 2—Étape 2. Investigations Géologiques, Géochimiques et Géophysiques Complémentaires, Synthèse des Résultats* (BRGM, 2008).

18. Feuillet, N. *MAYOBS1 French Oceanographic Cruise, RV Marion Dufresne* SISMER Database (French Oceanographic Fleet, 2019); https://doi.org/10.17600/18001217

19. *Transit valorisé de Mayotte à Brest* (SHOM, 2014); https://doi.org/10.17183/S201406900

20. Rubin, K. H. et al. Volcanic eruptions in the deep sea. *Oceanography* **25**, 142–157 (2012).

21. Chadwick, W. W. Jr et al. Recent eruptions between 2012 and 2018 discovered at West Mata submarine volcano (NE Lau Basin, SW Pacific) and characterized by new ship, AUV, and ROV data. *Front. Mar. Sci.* **6**, 495 (2019).

22. Clague, D. A. et al. Structure of Lō'ihi Seamount, Hawai'i, and lava flow morphology from high-resolution mapping. *Front. Earth Sci.* **7**, 58 (2019).

23. Cole, J., Milner, D. & Spinks, K. Calderas and caldera structures: a review. *Earth Sci. Rev.* **69**, 1–26 (2005).

24. Yeo, I. A. & Searle, R. High-resolution remotely operated vehicle (ROV) mapping of a slow-spreading ridge: mid-Atlantic ridge 45° N. *Geochem. Geophys. Geosyst.* **14**, 1693–1702 (2013).

25. Clague, D. A. et al. High-resolution AUV mapping and targeted ROV observations of three historical lava flows at Axial Seamount. *Oceanography* **30**, 82–99 (2017).

26. Bachelery, P. et al. Petrological and geochemical characterization of the lava from the 2018–2019 Mayotte eruption: first results. In *AGU Fall Meeting 2019* abstr. V52D–06 (AGU, 2019).

27. Cathalot, C. et al. Acoustic and geochemical anomalies in the water column around the newly formed volcano offshore Mayotte Island. In *AGU Fall Meeting 2019* abstr. V52D–05 (AGU, 2019).

28. Resing, J. A. et al. Active submarine eruption of boninite in the northeastern Lau Basin. *Nat. Geosci.* **4**, 799–806 (2011).

29. Baumberger, T. et al. Understanding a submarine eruption through time series hydrothermal plume sampling of dissolved and particulate constituents: West Mata, 2008–2012. *Geochem. Geophys. Geosyst.* **15**, 4631–4650 (2014).

30. Baker, E. T. et al. Hydrothermal discharge during submarine eruptions: the importance of detection, response, and new technology. *Oceanography* **25**, 128–141 (2012).

31. Chadwick, W. W. et al. Imaging of CO_2 bubble plumes above an erupting submarine volcano, NW Rota-1, Mariana Arc. *Geochem. Geophys. Geosyst.* **15**, 4325–4342 (2014).

32. Somoza, L. et al. Evolution of submarine eruptive activity during the 2011–2012 El Hierro event as documented by hydroacoustic images and remotely operated vehicle observations. *Geochem. Geophys. Geosyst.* **18**, 3109–3137 (2017).

33. Sohn, R. A. et al. Explosive volcanism on the ultraslow-spreading Gakkel ridge, Arctic Ocean. *Nature* **453**, 1236–1238 (2008).

34. Tarantola, A. Linearized inversion of seismic reflection data. *Geophys. Prospect.* **32**, 998–1015 (1984).

35. Anderson, E. Dynamics of formation of cone-sheets, ring-dikes, and cauldron subsidences. *Proc. R. Soc. Edinb.* 56, 128–157 (1937).

36. Nikkhoo, M., Walter, T. R., Lundgren, P. R. & Prats-Iraola, P. Compound dislocation models (CDMs) for volcano deformation analyses. *Geophys. J. Int.* **208**, 877–894 (2016).

37. Dofal, A., Fontaine, F. R., Michon, L., Barruol, G. & Tkalcic, H. Crustal structure variation across the southwestern Indian Ocean from receiver functions determined at Ocean-Bottom Seismometers. In *AGU Fall Meeting 2018* abstr. T43G0497 (AGU, 2018).

38. Merz, D., Caplan-Auerbach, J. & Thurber, C. Seismicity and velocity structure of Lō'ihi submarine volcano and southeastern Hawai'i. *J. Geophys. Res. Solid Earth* **124**, 11380–11393 (2019).

39. Wolfe, C., Okubo, P. & Shearer, P. Mantle fault zone beneath Kilauea Volcano, Hawaii. *Science* **300**, 478–480 (2003).

40. Ekström, G., Nettles, M. & Dziewoński, A. The global CMT project 2004–2010: centroid-moment tensors for 13,017 earthquakes. *Phys. Earth Planet. Inter.* **200**, 1–9 (2012).

41. Toda, S., Stein, R. & Sagiya, T. Evidence from the AD 2000 Izu Islands earthquake swarm that stressing rate governs seismicity. *Nature* **419**, 58–61 (2002).

42. Ágústsdóttir, T. et al. Strike-slip faulting during the 2014 Bárðarbunga-Holuhraun dike intrusion, central Iceland. *Geophys. Res. Lett.* **43**, 1495–1503 (2016).

43. Sigmundsson, F. et al. Segmented lateral dyke growth in a rifting event at Bárðarbunga volcanic system, Iceland. *Nature* **517**, 191–195 (2015).

44. Jacques et al. The ongoing Mayotte crisis suggesting reactivation of a caldera structure below the Moho. In *AGU Fall Meeting 2020* abstr. V040-0006 (AGU, 2020).

45. Gudmundsson, M. T. et al. Gradual caldera collapse at Bárdarbunga volcano, Iceland, regulated by lateral magma outflow. *Science* **353**, aaf8988 (2016).

46. Roche, O., Druitt, T. & Merle, O. Experimental study of caldera formation. *J. Geophys. Res. Solid Earth* **105**, 395–416 (2000).

47. Kumagai, H. et al. Very-long-period seismic signals and caldera formation at Miyake Island, Japan. *Science* **293**, 687–690 (2001).

48. Fazio, M., Alparone, S., Benson, P. M., Cannata, A. & Vinciguerra, S. Genesis and mechanisms controlling tornillo seismo-volcanic events in volcanic areas. *Sci. Rep.* **9**, 1–11 (2019).

49. Maeda, Y. & Kumagai, H. A generalized equation for the resonance frequencies of a fluid-filled crack. *Geophys. J. Int.* **209**, 192–201 (2017).

50. Sigmundsson, F. et al. Unexpected large eruptions from buoyant magma bodies within viscoelastic crust. *Nat. Commun.* **11**, 1–11 (2020).

51. Famin, V., Michon, L. & Bourhane, A. The Comoros archipelago: a right-lateral transform boundary between the Somalia and Lwandle plates. *Tectonophysics* **789**, 228539 (2020).

52. Armijo, R., Meyer, B., Navarro, S., King, G. & Barka, A. Asymmetric slip partitioning in the Sea of Marmara pull-apart: A clue to propagation processes of the North Anatolian fault? *Terra Nova* **14**, 80–86 (2002).

53. Dauteuil, O. & Brun, J.-P. Oblique rifting in a slow-spreading ridge. *Nature* **361**, 145–148 (1993).

54. Brune, S. Evolution of stress and fault patterns in oblique rift systems: 3-D numerical lithospheric-scale experiments from rift to breakup. *Geochem. Geophys. Geosyst.* **15**, 3392–3415 (2014).

55. Pagli, C., Yun, S.-H., Ebinger, C., Keir, D. & Wang, H. Strike-slip tectonics during rift linkage. *Geology* **47**, 31–34 (2019).

56. Franke, D. et al. The offshore East African rift system: structural framework at the toe of a juvenile rift. *Tectonics* **34**, 2086–2104 (2015).

57. Rufer, D., Preusser, F., Schreurs, G., Gnos, E. & Berger, A. Late Quaternary history of the Vakinankaratra volcanic field (central Madagascar): insights from luminescence dating of phreatomagmatic eruption deposits. *Bull. Volcanol.* **76**, 817 (2014).

58. Peacock, D. & Anderson, M. The scaling of pull-aparts and implications for fluid flow in areas with strike-slip faults. *J. Pet. Geol.* **35**, 389–399 (2012).

59. Pratt, M. J. et al. Shear velocity structure of the crust and upper mantle of Madagascar derived from surface wave tomography. *Earth Planet. Sci. Lett.* **458**, 405–417 (2017).

60. Mazzullo, A. et al. Anisotropic tomography around La Réunion Island from Rayleigh waves. *J. Geophys. Res. Solid Earth* **122**, 9132–9148 (2017).

61. Barruol, G. et al. Large-scale flow of Indian Ocean asthenosphere driven by Réunion plume. *Nat. Geosci.* **12**, 1043–1049 (2019).

62. Zhong, S. & Watts, A. Lithospheric deformation induced by loading of the Hawaiian Islands and its implications for mantle rheology. *J. Geophys. Res. Solid Earth* **118**, 6025–6048 (2013).

63. Watts, A. B. et al. Rapid rates of growth and collapse of Monowai submarine volcano in the Kermadec Arc. *Nat. Geosci.* **5**, 510–515 (2012).

64. Chadwick, W. W. Jr et al. A recent volcanic eruption discovered on the central Mariana back-arc spreading center. *Front. Earth Sci.* **6**, 172 (2018).

65. Schipper, C. I., White, J. D., Houghton, B., Shimizu, N. & Stewart, R. B. Explosive submarine eruptions driven by volatile-coupled degassing at Lōihi Seamount, Hawaii. *Earth Planet. Sci. Lett.* **295**, 497–510 (2010).

66. Carey, R. et al. The largest deep-ocean silicic volcanic eruption of the past century. *Sci. Adv.* **4**, e1701121 (2018).

67. Thordarson, T. & Self, S. The Laki (Skaftár Fires) and Grímsvötn eruptions in 1783–1785. *Bull. Volcanol.* **55**, 233–263 (1993).

68. Neal, C. et al. The 2018 rift eruption and summit collapse of Kīlauea volcano. *Science* **363**, 367–374 (2019).

69. Cogné, J.-P. & Humler, E. Temporal variation of oceanic spreading and crustal production rates during the last 180 My. *Earth Planet. Sci. Lett.* **227**, 427–439 (2004).

70. Marty, B. & Tolstikhin, I. N. CO_2 fluxes from mid-ocean ridges, arcs and plumes. *Chem. Geol.* **145**, 233–248 (1998).

71. Debeuf, D. *Étude de l'Evolution Volcano-Structurale et Magmatique de Mayotte, Archipel des Comores, Océan Indien: Approches Structurale, Pétrographique, Géochimique et Géochronologique.* PhD report, Reunion Univ. (2009).

72. Stamps, D., Saria, E. & Kreemer, C. A geodetic strain rate model for the East African Rift System. *Sci. Rep.* **8**, 732 (2018).

73. Deville, E. et al. Active fault system across the oceanic lithosphere of the Mozambique Channel: implications for the Nubia–Somalia southern plate boundary. *Earth Planet. Sci. Lett.* **502**, 210–220 (2018).

74. Macgregor, D. History of the development of the East African Rift System: a series of interpreted maps through time. *J. Afr. Earth Sci.* **101**, 232–252 (2015).

Methods

Summary. Ship-borne multibeam data were acquired using a Kongsberg EM122 1°×1° during the 2014[19] and 2019[18] oceanographic cruises. Ship-borne multibeam data were processed with the GLOBE software[75] to provide 30-m-grid spaced digital terrain models and seafloor backscatter imagery and to calculate depth differences, surface and volumes. The 3D acoustic water-column data from the 2019 cruise were processed using SonarScope (https://wwz.ifremer.fr/flotte_en/Facilities/Shipboard-software/Analyse-et-traitement-de-l-information/SonarScope) and GLOBE software[75]. A CTD rosette Seabird 911 equipped with an altimeter, an Aanderaa oxygen optode and a Seapoint turbidity meter was mounted on a carousel with 16 Niskin sampling bottles (8 l) to measure and sample throughout the water column. Subsampling was performed for onboard analyses (pH, alkalinity and total CO_2 by pH electrode and titration) and for onshore analyses (CH_4 analysis by the purge-and-trap method and H_2 and CO_2 analysis by the headspace method). For seismology, 800 earthquakes identified from the onshore catalogue were selected in descending magnitude order and manually picked on board. The seismic network used during the two-month deployment included OBSs and onshore local and regional stations (up to 500 km distance). The events were relocated with NonLinLoc[76] and a hybrid velocity model based on trials with six different velocity models, achieving final location accuracies better than 5 km. Eighty-four VLF earthquakes were detected between 25 February and 24 April 2019 using an amplitude trigger on ocean-bottom hydrophone recordings, filtered between 0.05 and 0.10 Hz, followed by a selection of events with a clear peak frequency and a final visual inspection. VLF earthquakes were located using spatial 3D back projection of station-pair cross-correlation functions[77], assuming a constant surface-wave speed of 3.5 km s⁻¹. A well-constrained epicentral location was obtained for 81 events. For geodesy, we inverted the surface deformation recorded by six permanent GNSS receivers installed in Mayotte, Grande Glorieuse and Madagascar. We used both an isotropic model and a triple volumetric discontinuities (pCDM source) in a homogeneous elastic half-space, isotropic material with Poisson's ratio of 0.25 to model the pressure source in depth. Seafloor pressure data (30 s sample interval) were pre-processed using harmonic analysis to remove the tides and low-pass filtering to remove residual oscillations interpreted as internal waves.

Ship-borne multibeam data: bathymetry and water-column acoustic data. We mapped the submarine slope and basin adjacent to Mayotte and detected and mapped water-column anomalies using ship-borne multibeam surveys over an area of 8,600 km² (Figs. 1–3, Extended Data Figs. 1–3 and Fig. 5). Bathymetric and seafloor backscatter datasets were collected in 2014 by the French SHOM[19] using the hydrographic and oceanographic vessel *Beautemps Beaupré*. The 2019 data[18] were collected using the research vessel *Marion Dufresne* during the MAYOBS1 cruise (3–18 May). Both vessels are equipped with identical Kongsberg EM122 multibeam echosounders (12 kHz, 1°×1° beam width). Bathymetry and seafloor backscatter datasets were processed using the GLOBE software[75] with identical 30-m-cell grids to allow accurate estimates of differences in depth, surfaces and volumes. Water-column acoustic data are available only for the 2019 cruise, and processing was performed using the SonarScope (@Ifremer) and GLOBE software packages using published methods[78].

Water column: sampling and chemical analysis. *Water-column sampling and in situ measurements with CTD rosette.* Seawater was sampled using IFREMER's CTD rosette, consisting of a Seabird 911+ CTD instrument mounted on a carousel with 16 8 l Niskin sampling bottles (Extended Data Fig. 4). For this cruise, the CTD rosette was equipped with an altimeter, an Aanderaa oxygen optode and a Seapoint turbidity meter. Information from the sensors was transmitted in real time to adapt the sampling strategy to observed water-column anomalies.

The Niskin bottles were subsampled for onboard and onshore analyses. For CH_4 analysis, 125 ml glass bulbs were used for analysis using the purge-and-trap method. The bulbs were allowed to overflow by at least two volumes of seawater, and particular care was taken to exclude air bubbles to prevent contamination. While filling, sodium azide was added to prevent future microbial activity. For H_2 and CO_2 analysis, 160 ml vials were filled using the headspace method. The vials, containing some sodium azide, were filled using a silicone tube connected to the Niskin bottle. The silicone tube was inserted to the bottom of the vial to completely fill the vial from the bottom to the top, displacing all contained air. The tube was then slowly removed, taking care to avoid any air bubbles, and the vial was sealed with a polytetrafluoroethylene septum using special crimping pliers. The headspace volume of 10 ml of atmospheric air was added using a needle mounted on a syringe.

CH_4 analysis by the purge-and-trap method at IFREMER laboratories. On shore, the purge-and-trap method[79] was used. Once in the laboratory, CH_4 was stripped from seawater using helium carrier gas, trapped on activated charcoal at −80 °C and detected and quantified with a flame ionization detector after separation on a packed column. Calibration was performed by injecting a commercial gas standard (CH_4 107.8 ppm). The limit of detection is 0.03 nmol l⁻¹, the precision (based on five replicates from the same rosette bottle) is within ±2% (confidence level 95%), and the accuracy is 5%. The CH_4 equipment was set up in a portable,

clean, air-conditioned container, allowing one CH_4 analysis every 6 min using two extraction kits.

The CO_2 and H_2 analyses were performed at IFREMER laboratories by a gas chromatography column coupled with a helium ionization detector following methods described in ref. [80], except that the headspace vial replaced the syringe.

pH, total alkalinity and ΣCO_2 measurements on board. The pH, total alkalinity and ΣCO_2 measurements were performed on board using a Metrohm 848 Titrino Plus titrator. The pH electrode was calibrated using commercially available pH buffers. The pH was measured as soon as possible after sample recovery, and total alkalinity and ΣCO_2 were then determined by direct titration with 0.1 N hydrochloric acid. Concentrations were compared with a seawater reference for oceanic CO_2 measurements (Batch 178).

Seismology data. The 800 earthquakes discussed in this paper were located using recordings from a network of up to 22 seismological stations equipped with sensors of different types, operating during different time slots between 25 February and 5 May 2019: 6 OBSs and up to 16 land stations on Mayotte Island, on Grande Glorieuse, on Khartala volcano, in Madagascar and in Kenya (Supplementary Information, Fig. 4 and Extended Data Figs. 6 and 8). Details on station location, type and quality are provided in Supplementary Figs. 2.1 and 2.2 and Supplementary Table 2.1.

An earthquake catalogue of 2,362 events of magnitude $2.0 < M < 5.4$, between 25 February and 5 May 2019, was produced in near real time by Bureau de Recherches Géologiques et Minières using land stations[81]. On board, three groups of operators working around the clock manually picked 800 of the events from the OBS, selected in descending magnitude order, using SeisComP3 software[82]. The Hypo71 software[83] was used for preliminary locations, and SeisComP3 was used to compute local magnitudes, the velocity model was updated to fit the data (see Supplementary Section 2) then the NonLinLoc software[76] was used to relocate the events. Low-frequency events were detected and analysed using the broadband land stations and the broadband hydrophone (HiTech HTI-90U, 30 s cut-off frequency) on the OBSs.

Geodesy data. We used the GNSS stations from the Centre National d'Etudes Spatiales (MAYG), EXAGONE's TERIA network (BDRL and GAMO), Precision Topo's Lel@ network (KAWE), IPGP (GLOR) and the Université de la Réunion (DSUA) (Supplementary Information and Extended Data Fig. 7). Seafloor pressure data were collected using Seabird SBE37 pressure sensors deployed on the OBS frames. The seawater pump of each instrument was deactivated to avoid induced noise on the seismometer recordings. Although SBE37s are not designed for seafloor geodesy, previous experiments indicate that their pressure gauge can be used to characterize sudden or large-amplitude deformations[84,85].

Data availability

The authors declare that most of the data supporting the findings of this study are available within the paper and its Supplementary Information files. GNSS data are available on the website (http://mayotte.gnss.fr) and can be downloaded from ftp://rgpdata.ign.fr/pub/gnss_mayotte/. Ship-borne geophysical data from the MAYOBS1 cruise can be obtained through the French national oceanographic data centre SISMER (http://en.data.ifremer.fr/SISMER, https://doi.org/10.17600/18001217), but restrictions apply to the availability of these data. The compilations of older bathymetric and topographic data are available on the SHOM website (http://www.shom.fr, https://doi.org/10.17183/S201406900). Rock samples are referenced at https://wwz.ifremer.fr/echantillons/Echantillons/Carte#/map (https://campagnes.flotteoceanographique.fr/prl?id=BFBGX-134187). Samples are accessible on site at IFREMER, Plouzané, France. Map were created using Globe software (https://doi.org/10.17882/70460)[75], ArcGIS software by Esri (https://www.arcgis.com/index.html), Generic Mapping Tools[86], Adobe illustrator (https://www.adobe.com/) and MATLAB. In addition to MAYOBS1 cruise multibeam data (resolution: 30 m)[18], Figs. 1, 2, 4, and 5 and Extended Data Figs. 1–3 and 6–9 include topographic and bathymetric compilation[16,87,88] (https://doi.org/10.17600/14000900, https://doi.org/10.17183), the General Bathymetric Chart of the Oceans (https://www.gebco.net) and global topography from SRTM GL1 (https://catalog.data.gov/dataset/shuttle-radar-topography-mission-srtm-gl1-global-30m); Litto3D Mayotte (https://diffusion.shom.fr/presentation/litto3d-mayot2012.html). Topography and bathymetry of Fig. 5b from GeoMapApp (www.geomapapp.org) CC BY. In Fig. 5 and Extended Data Figs. 6, 8 and 9, focal mechanisms for $M > 5$ earthquakes are from ref. [40]. In Fig. 5, $M > 2.5$ earthquakes are from ref. [4].

Code availability

Ship-borne multibeam data were processed with the GLOBE software[75]. The 3D acoustic water-column data were processed using SonarScope https://wwz.ifremer.fr/flotte_en/Facilities/Shipboard-software/Analyse-et-traitement-de-l-information/SonarScope and GLOBE software: https://doi.org/10.17882/70460[75]. GNSS solutions were computed using the GipsyX/JPL software available at https://gipsy-oasis.jpl.nasa.gov. Deformation source modelling codes (Mogi and Nikkhoo)

are available at https://github.com/IPGP/deformations-matlab, and data processing has been achieved using the WebObs open-source system available at https://ipgp.github.io/webobs/. Pressure-gauge data were processed with Python[89]. VLF event analysis has been performed using ObsPy[90], NumPy[91] and Matplotlib[92]. Earthquake phase picking was performed with SeisComP3[93], and initial locations used Hypo71[83]. Final locations were performed with NonLinLoc[76], and results were converted back to SeisComP3 using ObsPy[90].

References

75. Poncelet C., Billant G, & Corre M.P. *Globe (GLobal Oceanographic Bathymetry Explorer) Software* (SEANOE, 2020); https://doi.org/10.17882/70460

76. Lomax, A., Michelini, A. & Curtis, A. in *Encyclopedia of Complexity and Systems Science* (ed. Meyers, R.) (Springer, 2009); https://doi.org/10.1007/978-3-642-27737-5_150-2

77. Poiata, N., Satriano, C., Vilotte, J.-P., Bernard, P. & Obara, K. Multiband array detection and location of seismic sources recorded by dense seismic networks. *Geophys. J. Int.* **205**, 1548–1573 (2016).

78. Dupré, S. et al. Tectonic and sedimentary controls on widespread gas emissions in the Sea of Marmara: results from systematic, shipborne multibeam echo sounder water column imaging. *J. Geophys. Res. Solid Earth* **120**, 2891–2912 (2015).

79. Charlou, J. L., Dmitriev, L., Bougault, H. & Needham, H. D. Hydrothermal CH_4 between 12°N and 15°N over the mid-Atlantic ridge. *Deep Sea Res. A* **35**, 121–131 (1988).

80. Donval, J.-P. & Guyader, V. Analysis of hydrogen and methane in seawater by "Headspace" method: determination at trace level with an automatic headspace sampler. *Talanta* **162**, 408–414 (2017).

81. Bertil et al. *MAYEQSwarm2018: BRGM Earthquake Catalogue for the Earthquake Swarm Located East of Mayotte* (BRGM, 2018); http://ressource.brgm.fr/data/data/372c5809-3d30-440c-b44a-1c89385f176a

82. Hanka, W. et al. Real-time earthquake monitoring for tsunami warning in the Indian Ocean and beyond. *Nat. Hazards Earth Syst. Sci.* **10**, 2611–2622 (2010).

83. Lee, W. H. K. & Lahr, J. C. *HYPO71: A Computer Program for Determining Hypocenter, Magnitude, and First Motion Pattern of Local Earthquakes* (USGS, 1972).

84. Vilaseca, G. et al. Oceanographic signatures and pressure monitoring of seafloor vertical deformation in near-coastal, shallow water areas: a case study from Santorini caldera. *Mar. Geod.* **39**, 401–421 (2016).

85. Fox, C. G. In situ ground deformation measurements from the summit of Axial volcano during the 1998 volcanic episode. *Geophys. Res. Lett.* **26**, 3437–3440 (1999).

86. Wessel, P. & Smith, W. H. New, improved version of Generic Mapping Tools released. *Eos* **79**, 579–579 (1998).

87. *MNT Bathymétrique de la Façade de Mayotte* (SHOM, 2016); https://doi.org/10.17183/MNT_MAY100m_HOMONIM_WGS84

88. Jorry, S. *PTOLEMEE French Oceanographic Cruise, RV L'Atalante* SISMER database (French Oceanographic Fleet, 2014); https://doi.org/10.17600/14000900

89. Van Rossum, G. & Drake, F. L. *Python Reference Manual* (iUniverse, 2000).

90. Krischer, L. et al. ObsPy: a bridge for seismology into the scientific Python ecosystem. *Comput. Sci. Discov.* **8**, 014003 (2015).

91. Harris, C. R. et al. Array programming with NumPy. *Nature* **585**, 357–362 (2020).

92. Hunter, J. D. Matplotlib: a 2D graphics environment. *Comput. Sci. Eng.* **9**, 90–95 (2007).

93. Weber, B. et al. SeisComP3—automatic and interactive real time data processing. *Geophys. Res.* **9**, 219 (2007).

Author contributions

N.F., S.J., W.C.C., C.D., I.T., E.J., J.M.S., A. Lemoine, F.P., R.D., A.G., C.A., O.F., P.K., A. Laurent, J.-P.D., L.G., J.G., V.G., P.P. and E.R. participated on the MAYOBS1 cruise (N.F., S.J. and W.C.C. as principal investigators), acquired and processed the geophysical and seismological data. C. Satriano, A. Laurent and P. Bernard. detected and located the VLF events. A.P. was in charge of the GNSS installation in Glorieuse Island and processed and modelled the GNSS data with F.B. and R.G. V.B. was in charge of the APGs installed on the OBSs and processed their data. S.B. participated in the first OBS deployment on the *Ylang* vessel with W.C.C. and R.D. D.B., A. Lemarchand and J.V.d.W. were responsible for the installation of new seismological and GNSS stations in Mayotte and for data acquisition on shore. J.-P.D., V.G., E.R. and C.C. performed the geochemical analysis and interpretation of the water-column data. C. Scalabrin and A.G. processed the EM122 acoustic data. C.D. and A.G. performed the depth changes calculation. C. Scalabrin provided the interpretation of the water-column acoustic data. P. Bachelery and Y.F. furnished the rock sample descriptions and petrological analysis. N.F., S.J., C.D., P. Bachelery, Y.F., I.T., F.P., J.V.d.W. and E.J. provided the geological interpretation. N.F. wrote the paper with the contribution of all other authors. P. Bernard, J.M.S., E.J., W.C.C., C. Satriano, P. Bachelery, A. Lemoine, A. Laurent, C.A., V.B., A.G., A.P., F.B., R.G., E.R., C.C. and C. Scalabrin wrote the Methods section and the Supplementary Information.

Competing interests

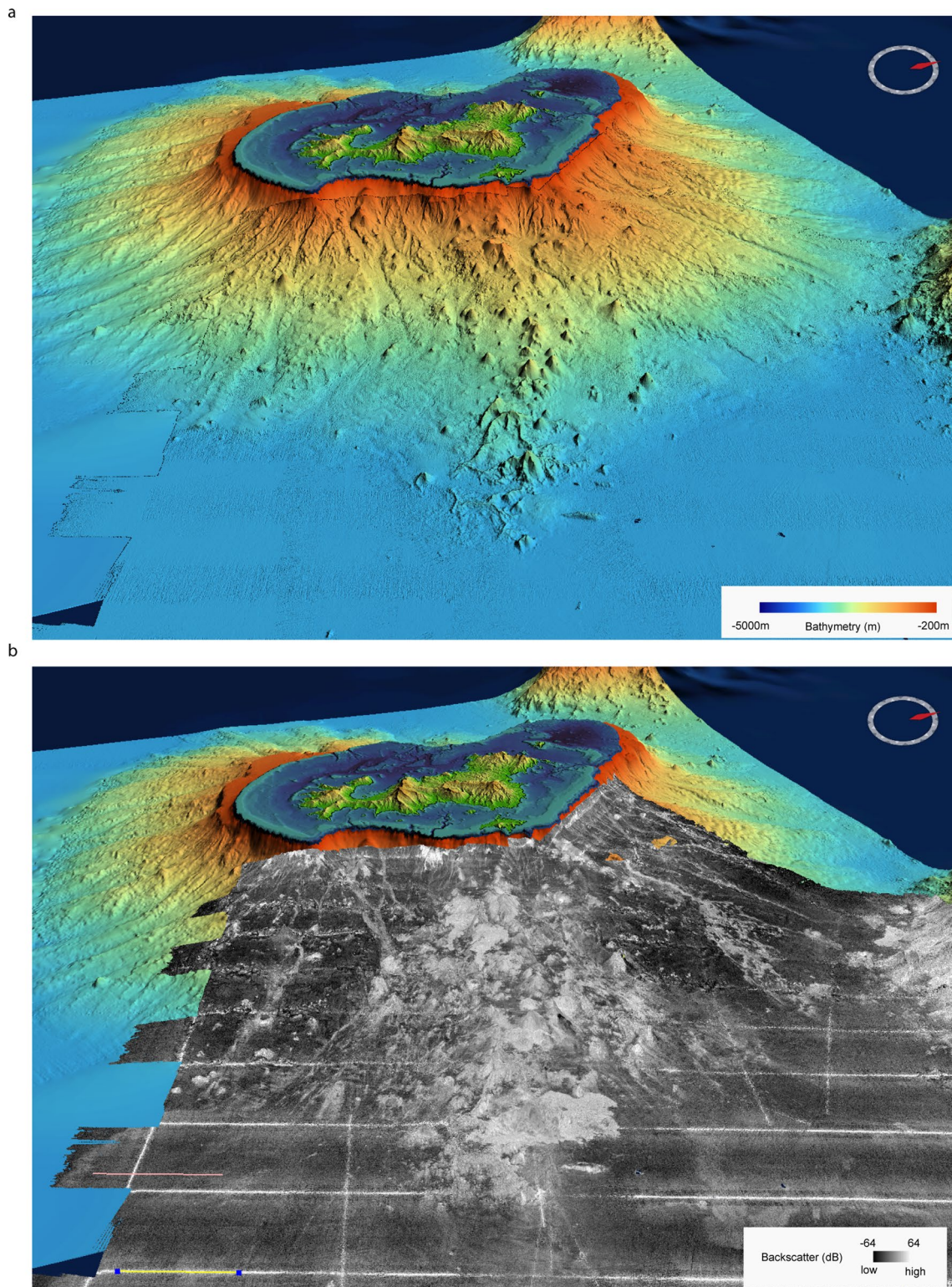The authors declare no competing interests.

Additional information
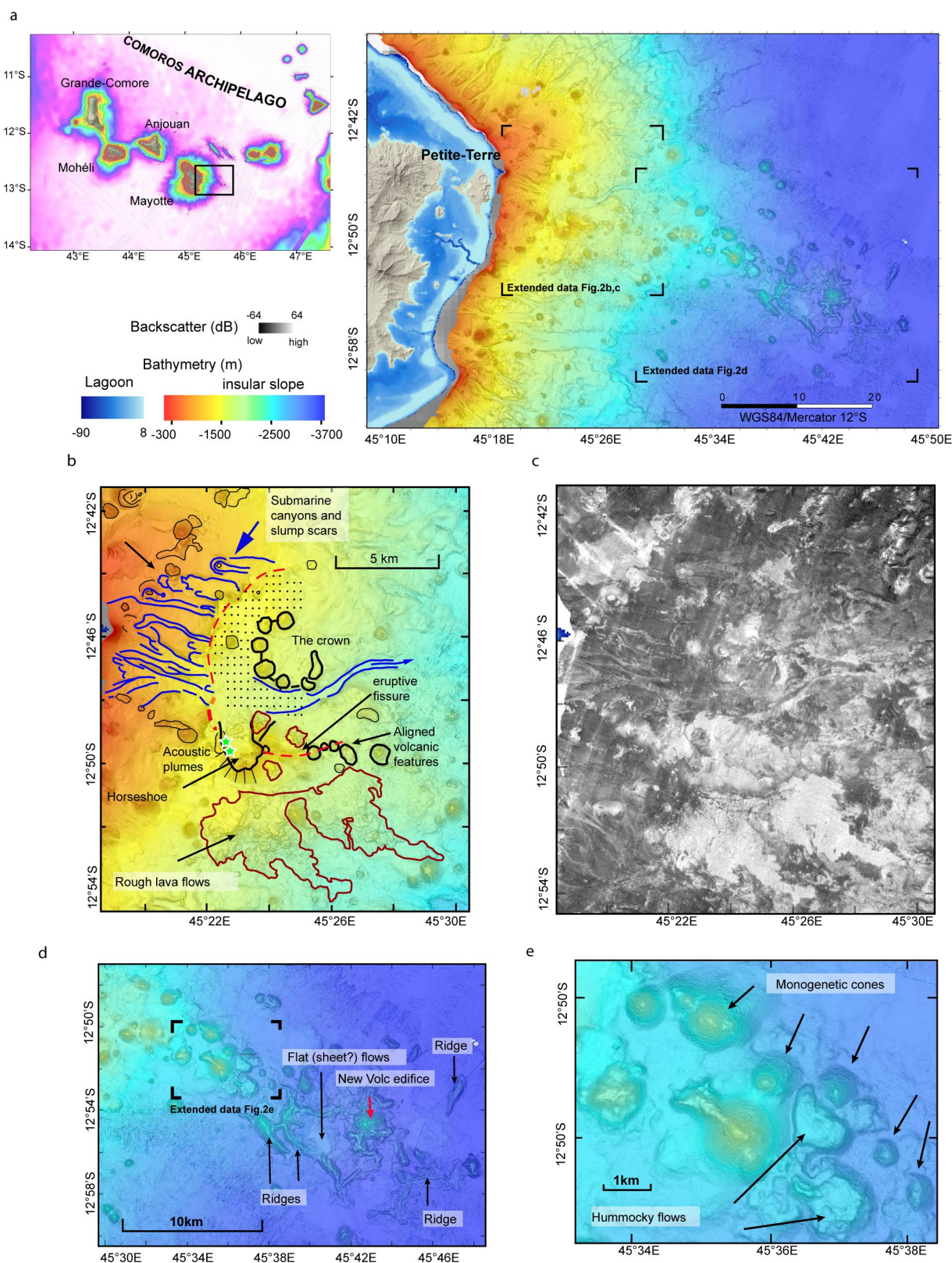
Extended data is available for this paper at https://doi.org/10.1038/s41561-021-00809-x.

Supplementary information The online version contains supplementary material available at https://doi.org/10.1038/s41561-021-00809-x.

**Correspondence and requests for materials** should be addressed to N.F.

Peer review information *Nature Geoscience* thanks Kenneth Rubin and Cynthia Ebinger for their contribution to the peer review of this work. Primary Handling Editor: Stefan Lachowycz.

Reprints and permissions information is available at www.nature.com/reprints.

Extended Data Fig. 1 | The Mayotte Ridge. 3-D westward view of submarine volcanic features located east of Mayotte. **a**) Bathymetry from MAYOBS1 30-m resolution DTM and[16,87] (3x vertical exaggeration) (**b**) Backscatter seafloor reflectivity (white is highest reflectivity) from MAYOBS1 cruise.

Extended Data Fig. 2 | Volcanic features offshore Mayotte. a) 30-m resolution EM122 multibeam bathymetry (MAYOBS 1 cruise) and[16,87] with locations of Fig. 2. b,c,d indicated. **b**), **c**) Interpreted MAYOBS1 shipboard bathymetry and backscatter of the upper slope east of Mayotte (location in **a**). Cones, lava flows and canyons as in Fig. 1b. Black dots: bathymetric depression. Dashed red lines: pre-existing caldera structure. **d**) Interpreted bathymetry of the lower slope east of Mayotte (localisation in **a**). **e**) zoom on **d**) showing monogenetic cones and lava flows.
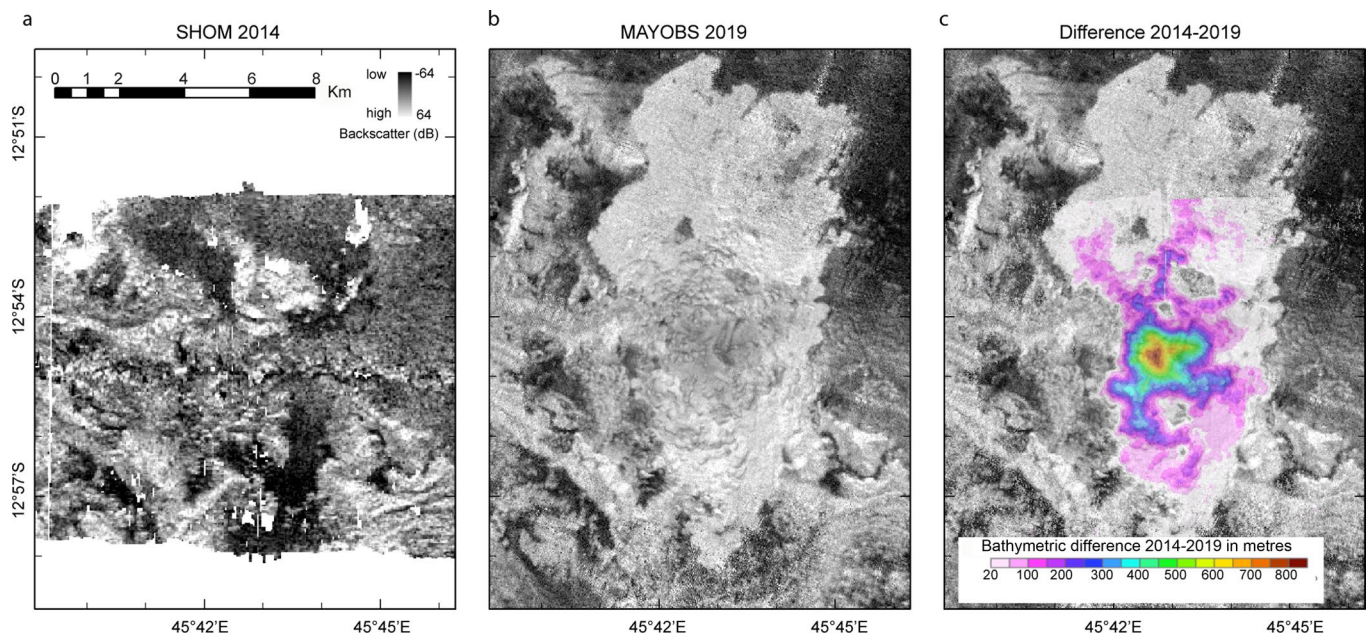
Extended Data Fig. 3 | The new volcanic edifice. a) 2014 EM122 multibeam seafloor backscatter[19]. **b**) 2019 reflectivity (MAYOBS 1 cruise)[18]. c) Depth changes between the 2014 and 2019 surveys, superimposed on 2019 reflectivity. The white areas of the 2019 backscatter map exceeding the bathymetric difference map indicate the extent of new volcanic material.
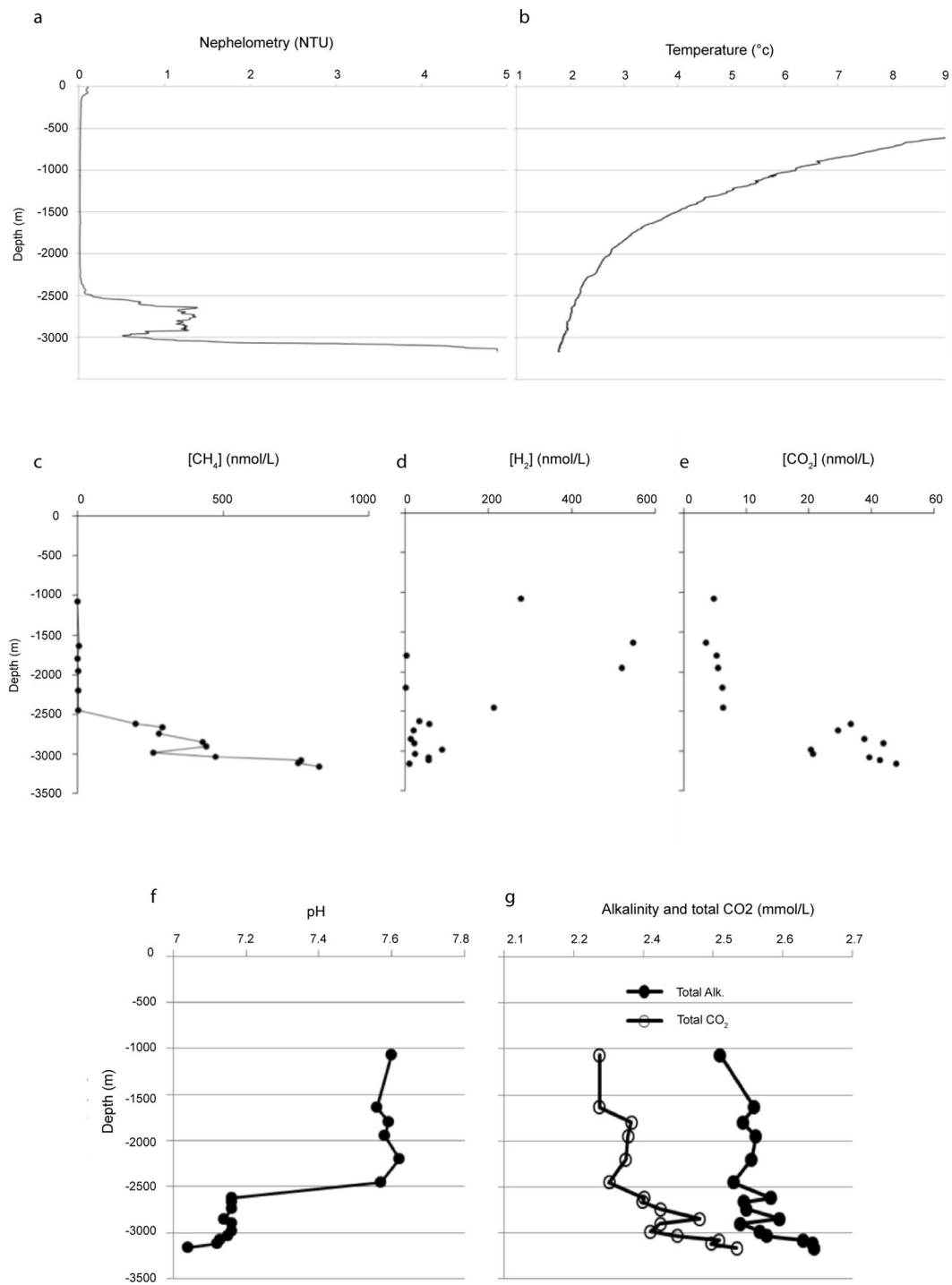
Extended Data Fig. 4 | CTD (conductivity temperature-depth)-Rosette measurements. a) Nephelometry and **b**) temperature vertical profiles. **c**–**g**) sample analyses from 8L ®Niskin bottles. **c**–**e**) Gas concentrations(CH_4, H_2, CO_2); **f**) pH, **g**) total alkalinity and total CO_2.

a

b
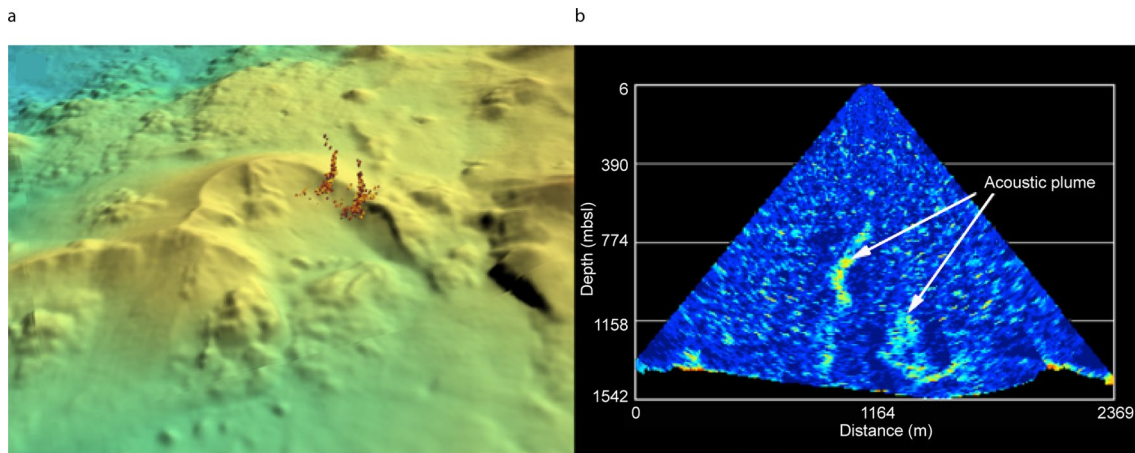
Extended Data Fig. 5 | Acoustic plumes over the Horseshoe volcanic structure. a) Southward 3D view of the horseshoe morphology and two water column acoustic plumes observed on the western internal flank. **b**) Processed polar echogram from one EM122 multibeam ping of the data set displayed in (**a**) acquired on May 18th (05:41 UT) horizontal and vertical-axes correspond respectively to the cross-track distance and the water depth, in meters) – see also Acoustic plume movie 2.
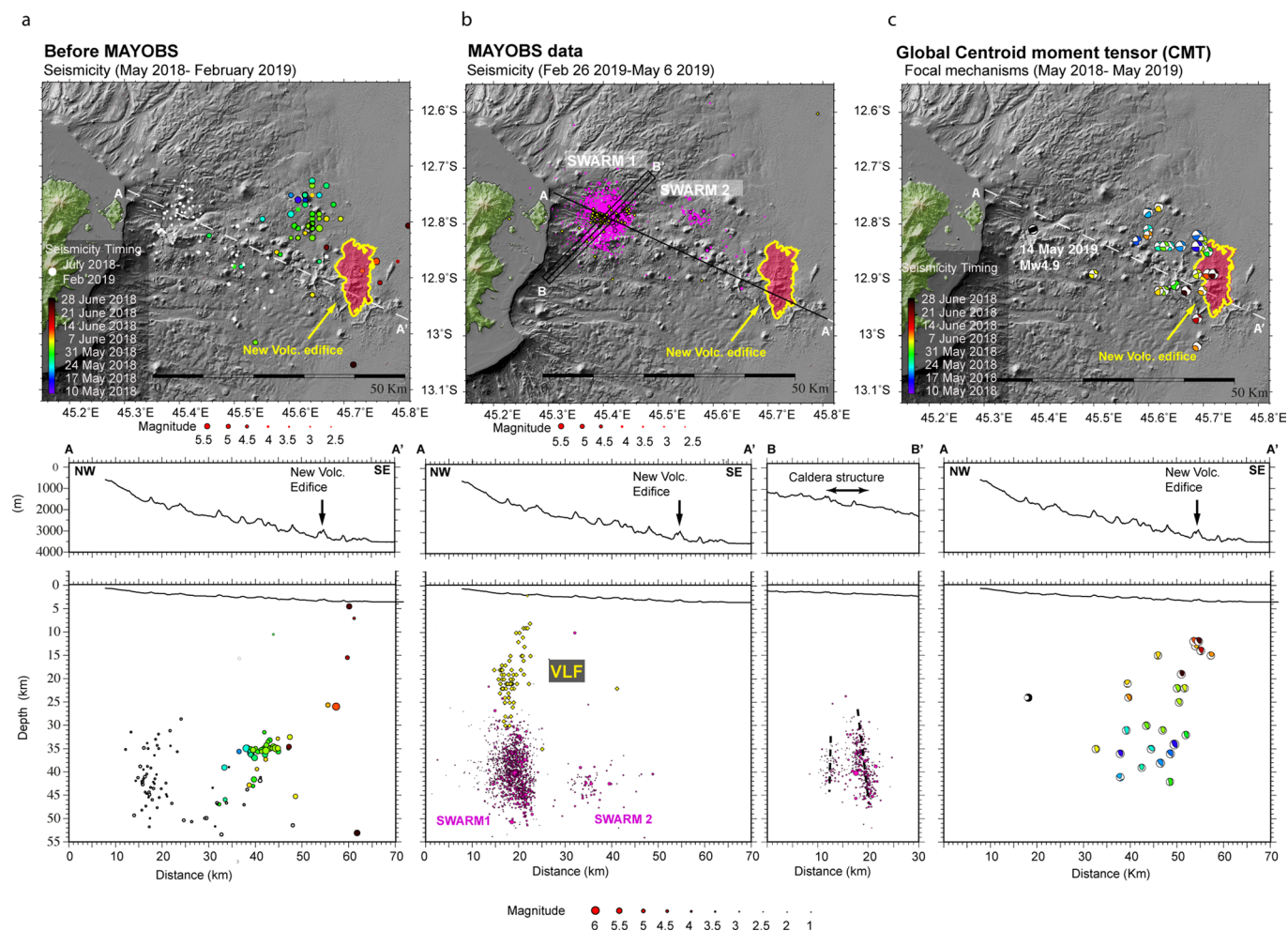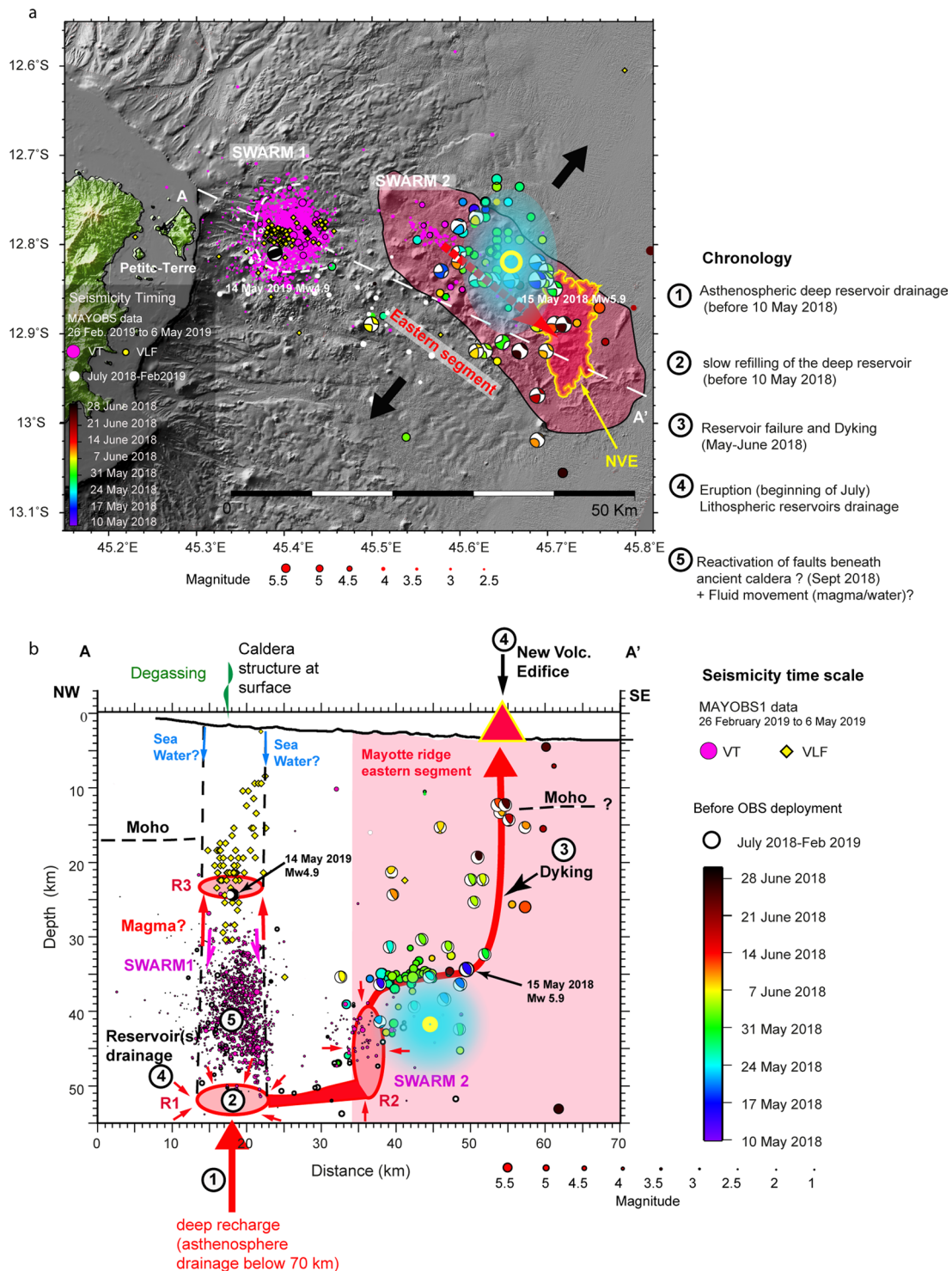
Extended Data Fig. 6 | Seismicity. Top: map views, bottom: cross-sections (A-A') projection along azimuth N115°E; (B-B') along azimuth N45°E. **a**) Earthquakes recorded by onshore seismological stations before the deployment of the Ocean bottom seismometers (OBS). Colored circles are events occuring in the first six weeks of the crisis, white circles are earthquakes in the intervening 8 months. **b**) Earthquakes recorded by the OBS+land stations between February 25 and May 6 2019 (pink dots). Yellow diamonds: location of the Very Low Frequency (VLF) events located in this study (see supplementary 2.3). **c**) Focal mechanisms of the largest earthquakes from the Harvard CMT catalog[40] with color scale as in **a**).
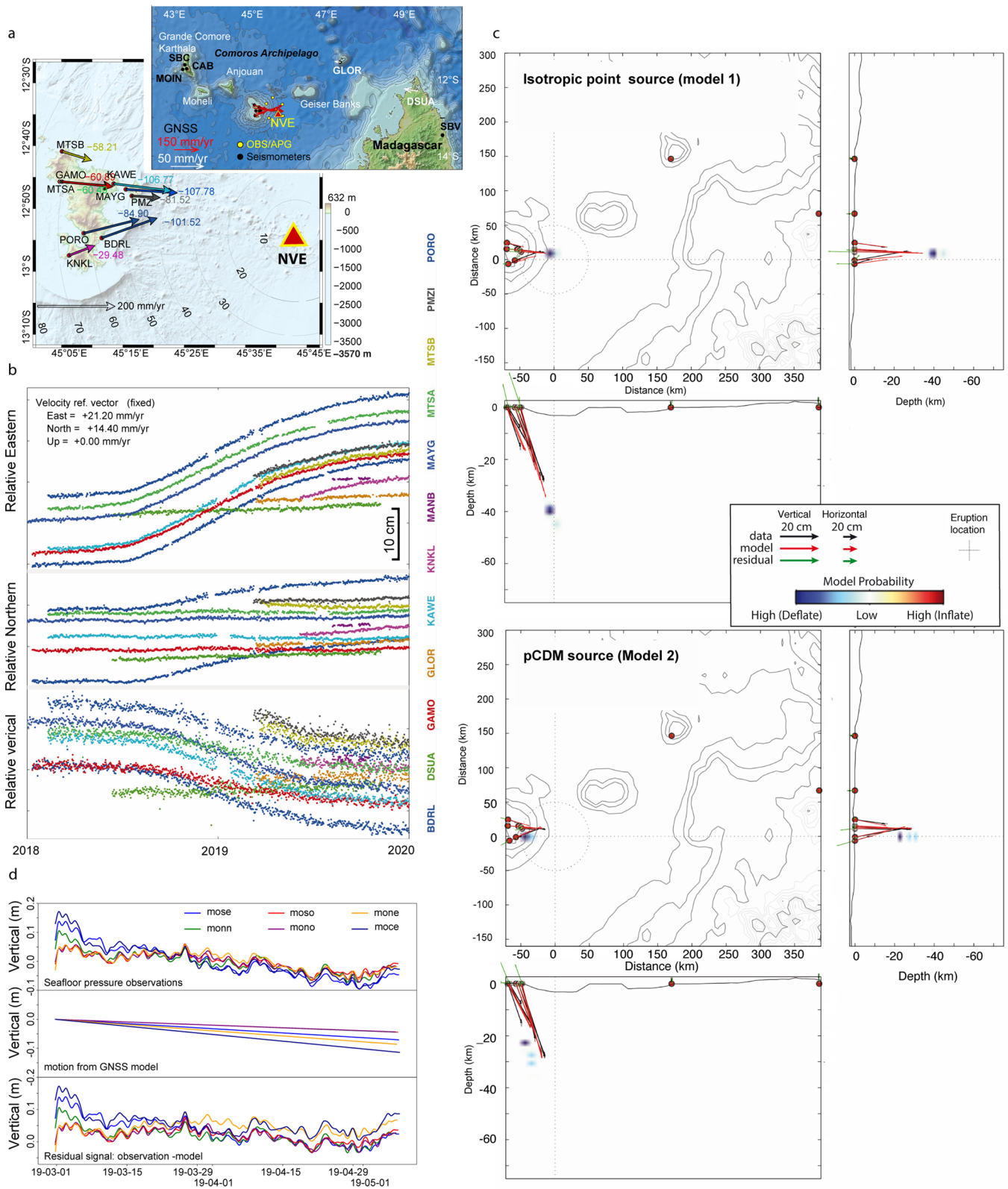
Extended Data Fig. 7 | See next page for caption.

Extended Data Fig. 7 | Global Navigation Satellite System (GNSS) data modelling and seafloor subsidence estimated from seafloor pressure variations. a) Stations locations. Arrows with colors and names: GNSS velocity vectors (mm/yr) and station names. Coloured numbers: vertical deformation (mm/yr). Inset: yellow dots : pressure sensors on ocean bottom seismometer stations (see supplementary Fig. 2.1), red arrows: Mayotte GNSS velocity vectors (mm/yr), white arrows: far field GNSS velocity vectors. **b)** GNSS Time series with relative displacements recorded on the east (top), north (middle) and vertical (bottom) components of the stations between January 2018 and January 2020. **c)** Best fit-models with 1σ uncertainties of the GNSS data for one isotropic point source and a triple volumetric discontinuity pCDM source. **d)** Top panel: Pressure recorded by Seabird SBE37 gauges at the six ocean-bottom seismometer stations (Yellow dots inset Figure 7a and supplementary Fig. 2.1) de-tided and converted to vertical motion. Middle panel: vertical deformation estimated at each seafloor instrument location, using the best isotropic source model obtained from the GNSS data for the March 1st to May 1st 2019 period.

Extended Data Fig. 7 | Global Navigation Satellite System (GNSS) data modelling and seafloor subsidence estimated from seafloor pressure variations.

Extended Data Fig. 8 | Conceptual model for the Mayotte seismo-volcanic event. Circles and diamonds are events as in Extended Data Fig. 6. Focal mechanisms of main earthquakes are from Harvard CMT catalog[40]) with the same color scale as the May 10 to June 30, 2018 Volcano-Tectonic (VT) earthquakes, Yellow circle and blue patch: Location, with 3 sigma uncertainties, of the most robust isotropic source deformation model. **a**) Map view: The redish ellipse: Mayotte ridge, dashed circular area: old caldera structure in the morphology. Double black arrows: local extension Dashed red arrow: dyke intrusion **b**) Cross-section (projection along azimuth 115 degree, location on **a**)). Symbols as in **a**). Red lines: magma migration (dykes). Red ellipses and circle: magma reservoirs or mushes. Pink arrow: possible downsag along caldera structures. Redish zone: Eastern segment of the Mayotte ridge.
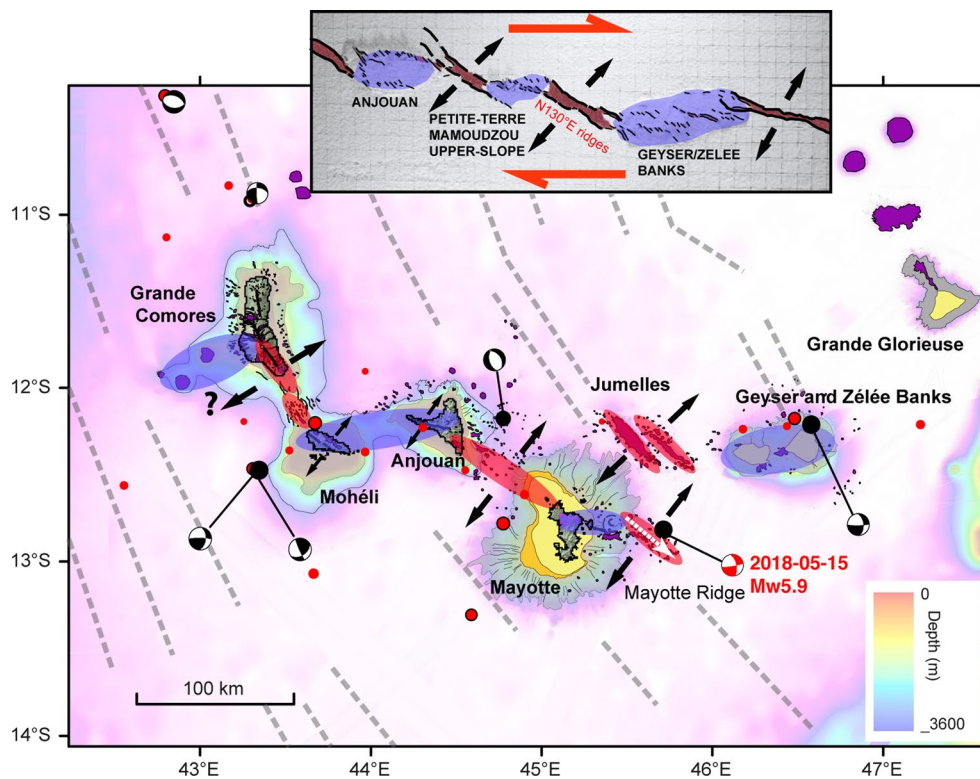
Extended Data Fig. 9 | Regional volcano-tectonic setting of the submarine eruption offshore Mayotte. a) Volcano-tectonic setting of the new volcanic edifice (NVE). Volcanic cones and ridges (purple) from this study and[13,16,51,71]. Beach balls: focal mechanisms for M>5 earthquakes[40]. Dotted white arrow: dyking event along the N130° E trending eastern segment of the volcanic ridge. Pink ellipse: inferred main volcano-tectonic ridges. Purple ellipses: highly damaged zones in between the en echelon ridges. Dashed grey lines: Mesozoic fracture zones[6]. Inset: sandbox model adapted from[58] illustrating the possible arrangement of the main volcano-tectonic structures in Comoros. Thick black arrows: local extension direction.